Research on Late-Robust Combustion

by

Craig B.E. Wildman

B.S., Mechanical Engineering
Massachusetts Institute of Technology, 2003

Submitted to the Department of Mechanical Engineering in Partial Fulfillment of the
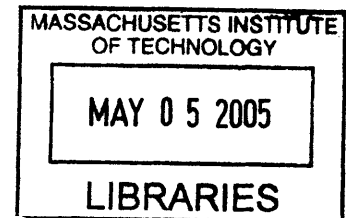Requirements for the Degree of

Master of Science in Mechanical Engineering

at the

Massachusetts Institute of Technology

February 2005

Signature of Author

Department of Mechanical Engineering
January 25, 2005

Certified by_____
Wai K. Cheng
Professor of Mechanical Engineering
Thesis Advisor

Accepted by_____
Lallit Anand
Professor of Mechanical Engineering
Chariman, Department Graduate Committee

BARKER

1

(This page was intentionally left blank.)

Research on Late-Robust Combustion

by

Craig B.E. Wildman

Submitted to the Department of Mechanical Engineering on
January 25, 2005 in partial fulfillment of the
requirements for the Degree of Master of Science in
Mechanical Engineering

Abstract

To better understand the role that turbulence plays in causing cycle-by-cycle variations, an experimental study was carried out in which charge motion or laminar flame speed was varied. Two sets of tests were done. The first consisted of using an air jet mounted in the intake port to generate charge motion at a spark-timing sweep from 20° BTC to 20° ATC. Two jet orientations were tested with the intent of generating swirl and tumble. Also done over this spark-timing sweep, the second set of tests consisted of replacing the nitrogen in air with a diluent, argon or carbon dioxide, to increase or decrease, the laminar flame speed. Tests were conducted at fast-idle conditions. These were 2.6bar NIMEP, 1400rpm, 20°C average coolant temperature, and relative air-fuel ratio set to 1.00.

In-cylinder pressure measurements yielded COV of NIMEP and burn duration. Exhaust temperature was also recorded. The swirl jet improved COV of NIMEP a maximum of approximately 30% at each spark timing tested. The tumble jet improved COV a maximum of 10% to 44% depending on the spark timing. No jet flow increased or decreased exhaust temperature more than approximately 5%. Strong correlation was found between exhaust temperature and combustion phasing. The turbulence test data showed a correlation between exhaust temperature and COV as well as between COV and combustion phasing. However, the change in laminar flame speed data showed a weaker correlation in both.

Thesis Supervisor: Wai K. Cheng
Title: Professor of Mechanical Engineering

(This page was intentionally left blank.)

Acknowledgements

As I worked on the Master of Science degree over the last year and a half, I learned a great deal about doing research and about life in general. During this time I received advice, help, and good examples from a number of people around me.

Professor Wai Cheng, my thesis advisor, certainly gave advice on a wide range of topics regarding research and life; however, he influenced me mostly through his example. His attitude around me was continually positive, as he showed patience and good humor during my reports of mistakes or test failures. Also, he was exceptionally available and always willing to go down to the lab to examine the details of an issue. Because he did small amounts of lab work with me, he opened a venue for directly teaching proper habits. Finally, I noticed his conscious effort to spend time with students when we went out as a group.

Thane DeWitt, the laboratory manager, was very helpful dealing with the practical matters of building an experimental apparatus. Thane taught me a wide variety of practical lessons. I also appreciated his congenial nature and his way of adding fun into work. This seemed to set a tone with others in lab.

The community in lab was very supportive and helpful, as well. Brian Hallgren, Jeff Mathews, Halim Santoso, Mike Gerty, Morgan Andreae, Dong-Kun Lee, Kevin Lang, Tony Zhang, Ferran Ayala, Devon Manz, Jeff Jocsak, Steve Przesmitzki, Jim Cuseo, and others all helped with lab work or class work. From the help and example of these people, I became a better, more professional researcher in ways ranging from building electronics to understanding the hierarchy of academia. Also, the students in the Sloan Lab, along with the staff and faculty, made lab into a community, which helped me to be passionate about research and which kept life enjoyable.

Before coming to MIT and during my time here, my family has been continually supportive and has been as helpful as it could be. I am thankful for the opportunities and the motivation that my parents and my brother gave me during my life.

Table of Contents

List of Figures

List of Tables

Nomenclature and Symbols

NVH: noise-vibrations-harshness
CCV: cycle-by-cycle variations
NIMEP: net indicated mean effective pressure
COV: covariance
HC: unburned hydrocarbons
FTP: Federal Test Procedure
MBT: maximum brake torque
GIMEP: gross mean effective pressure
AFR: air-fuel ratio
MAP: manifold air pressure
CAD: crank angle degree
TC: top center
BC: bottom center
BTC: before top center
ATC: after top center
BBC: before bottom center
ABC: after bottom center
IVO: intake valve open
IVC: intake valve close
EVO: exhaust valve open
EVC: exhaust valve close
RPM: revolutions per second
CA: crank angle

Chapter 1 Introduction

1.1 Overview

Cycle-by-cycle torque variations in a spark ignition engine is a phenomenon that is not fully understood, and it affects the noise-vibrations-harshness (NVH) quality of the engine. These variations are caused by variations in charge motion, by variations in the mixture inhomogeneity in temperature and concentration, by variations in the amounts of the reactants, and by variations in the spark discharge. The relative dependence on each of these mechanisms is still being explored [1].

Increasing cycle-by-cycle variations (CCV), in general, results in several adverse effects. The effects of high CCV are most noticeable in increased engine noise and poor drivability caused by increased speed and torque fluctuations. Aside from reducing drivability, to suppress the speed and torque fluctuations at idle also requires a higher engine idle speed, which results in higher fuel consumption. Because some cycles feature a substantially slower burn rate than optimized, incomplete combustion may occur, resulting in high fuel consumption as well as higher HC emissions. At high loads, the cycles that feature higher a octane requirement than average force the engine to operate further from the average cycle's knock limit [2]. In general, reducing CCV allows the engine to be operated closer to its average operating limits [3].

The work herein seeks to develop greater understanding of the causes of cycle-by-cycle torque variations by studying the effects of changing fluid motion and laminar flame speed. A variable air jet in the intake port is used to vary in-cylinder turbulence whereas substitution of the nitrogen of the air supply by carbon dioxide and argon, respectively, is used to vary the laminar flame speed of the charge mixture. Relationships between burn duration, combustion phasing, exhaust gas temperature, and covariance (COV) of net indicated mean effective pressure (NIMEP) are explored.

1.2 Motivation

Using a catalytic converter for aftertreatment is an effective way to eliminate a great deal of the unburned hydrocarbons (HC) in the exhaust of a spark ignition engine. However, the catalyst is ineffective before it reaches a critical temperature ($\sim 300°C$). Consequently, a substantial portion of the total HC emissions produced in the Federal Test Procedure (FTP-75)

occurs during the first few minutes of engine operation after the cold start before the catalyst reaches light-off temperature. Approximately 75% of the tailpipe HC emissions occur in the first two minutes of operations; while the engine-out HC emissions are only 20% of the total engine-out emissions [4].

Substantial HC emission reductions can be realized by quickly heating the catalyst during engine start so that it is effective for a longer percentage of engine operation. One strategy to accomplish this is to increase the exhaust temperature by retarding the spark timing [5]. Late combustion results in a high exhaust temperature. The charge does less work on the piston, and there is less time for heat transfer from the burned gas into the cylinder walls.

Two notable side effects occur when spark timing is significantly retarded. First, HC emissions are substantially reduced. Since the exhaust is hotter, more HC oxidation takes place during the exhaust event and in the exhaust system than when the timing is close to MBT timing. Russ et al. observed decreasing HC concentration measured in the exhaust port as timing is retarded. Also, they observed the amount of burn-up in the exhaust system greatly increased [6]. Hallgren and Heywood observed similar results of HC burn-up in the exhaust manifold runner and other parts of the exhaust system [7].

Retarding the spark timing also has the effect of increasing cycle-by-cycle torque variations, especially at low load and low speed. Since the heat release of the mixture is not optimally timed with compression, the peak cylinder pressure and the flame temperature are lower than for combustion begun at maximum brake torque (MBT) timing. Consequently, laminar flame speed is lower. Also, at a later ignition timing, turbulent fluid motion has decayed more since its inception during the intake event. Because both the laminar and the turbulent flame speeds are decreased, burn duration increases, and more time is allowed for cycle-by-cycle variations in the turbulent motion of the mixture to affect flame propagation. Allowing more time for chaotic processes results in a higher likelihood of variations in the pressure profile and the torque [5]. Furthermore, when combustion occurs late, the indicated torque is much more sensitive to combustion phasing.

Nissan Motor Company, the sponsor of the project, wishes to further understand the mechanism for generating cycle-by-cycle torque fluctuations. It intends to use a spark-retard strategy at engine start to accelerate catalyst light-off. It must mitigate the increased CCV so that drivability is not sacrificed with this fast-light-off strategy. A probable start-up schedule would

consist of initially bringing the engine speed above 2000rpm to ensure consistent starting. Then, immediately reduce engine speed to a fast idle, about 1400rpm, at which point the timing is retarded to heat the exhaust and light off the catalyst. This fast idle is used to increase the mass flow through the engine for faster heat up of the exhaust system than a normal idle speed would do.

After the catalyst light-off, the spark timing would be advanced to normal idle timing, and the engine would reduce speed to the normal 600-800rpm to conserve fuel.

Chapter 2 Combustion Process and Sources of Cycle-by-cycle Variations

To better understand test results, the engine combustion process will be briefly described, and the primary causes of cycle-by-cycle torque variations will be explained. In a spark ignition engine, premixed fuel and air are compressed then ignited by a voltage breakdown in a spark plug. A spherical flame kernel develops and propagates outward. As the flame radius increases, the reaction zone becomes increasingly wrinkled and folded through turbulent fluid motion until the flame reaches the cylinder wall. The process can be divided into four stages: the flame initiation stage, the flame development stage, the flame propagation stage, and the flame termination stage. The flame initiation stage consists of the spark discharge and ignition. The flame development stage is defined as the time for a small but significant amount of charge to burn, typically at 10% of the total mass burned. Next, the flame propagation stage comprises the burn from the end of the flame development stage to the point where a significant part of the fuel has been consumed; this stage corresponds typically to the evolution of 10%-90% of the burned mass fraction. The flame termination stage is where the final 10% of the charge burns; however, as much as 25% of the charge can burn after the flame reaches the cylinder wall [5]. The causes of CCV will be examined in the first three sections. Cyclic torque variations are not ascribed to the fourth stage so it will not be considered [3].

CCV are caused by four separate sources during combustion: fluid motion, mixture inhomogeneity, mixture composition variations, and variations in spark characteristics. Fluid motion comprises fluctuations in large-scale motion and variations in the level of small-scale turbulence [1]. Variations in the amount of each component of the mixture affect the speed and total heat release during combustion. Finally, variations in spark characteristics, such as in the discharge schedule, affect the amount of energy delivered to the initiated flame kernel. With a modern ignition system, this effect is not significant [2].

2.1 Large-Scale Charge Motion

In-cylinder charge motion displays a mean velocity and a turbulent intensity at every point in the cylinder, and there are cycle-by-cycle variations of each one because of the turbulent nature of the flow. Described in Equation 2-1 and explained further in Appendix A, the instantaneous velocity at a point can be defined by three components. First, there is an ensemble-average velocity at the crank angle of many cycles $\overline{U}_{EA}(\theta)$. Then, there is lower frequency mean

velocity for a particular cycle $\hat{U}(\theta,i)$, and a term to describe the random fluctuations u at a higher frequency.

$$U(\theta,i) = \overline{U}_{EA}(\theta) + \hat{U}(\theta,i) + u(\theta,i) \qquad (2\text{-}1)$$

Fluctuations in large-scale charge motion represented by the variations of $\hat{U}(\theta,i)$ cause CCV in three mechanisms of varying importance: spark channel stretch, flame kernel displacement, and mean-flow variations during the propagation stage. High frequency fluctuations, represented by the fluctuations of u, affect the turbulent entrainment process and thus the burn rate.

2.1.1 Spark Channel Stretch

Mean velocity can stretch the discharge channel if it is strong enough. The energy transfer to the gas consists of the heat loss to the electrodes and the ignition circuit discharge rate. Since the energy transfer depends on the geometry of the discharge, the local velocity at the spark plug may substantially alter the discharge characteristics.

2.1.2 Kernel Displacement

During the flame development stage a small, yet significant amount of the charge is reacted, often considered 10% of the total burned mass. This stage is especially significant to combustion stability because the random variations in this early part of the combustion process have been found to be much larger than variations during later stages of combustion [8].

Fluctuations in flame kernel displacement significantly contribute to CCV in burn duration and, hence, in NIMEP. Even under quiescent conditions in an engine, there is a finite flow velocity in the vicinity of the spark plug gap that moves the flame kernel relative to the gap. The distance from the flame initiation point to the furthest part of the cylinder wall defines how far the flame must travel. In a chamber with one spark plug, if the flame kernel is blown toward the center of the cylinder, the burn duration will be shorter than if it is blown away from the cylinder center as depicted in the diagram in Figure 2-1.

Spark Plug   Flame Kernel   Spark Plug

Fast Burn   Flame Kernel   Slow Burn
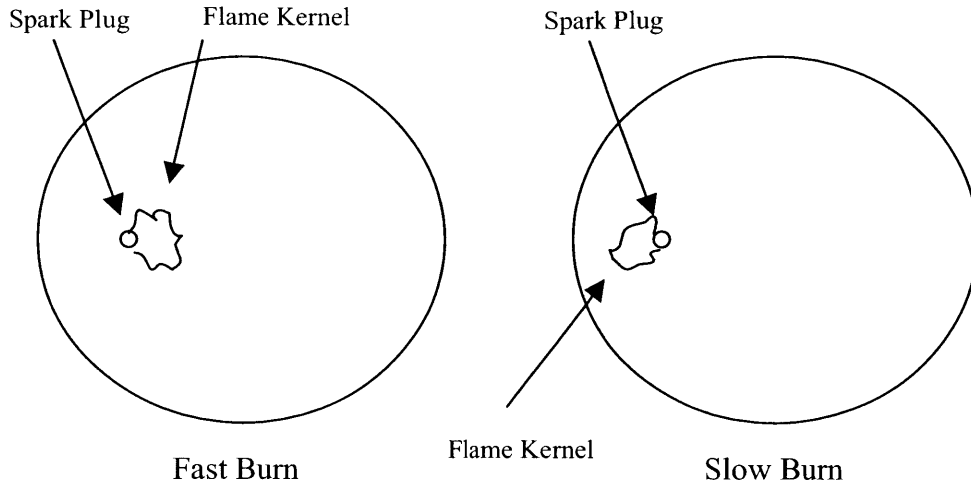
Figure 2-1   **Chamber Plan View of Kernel Displacement. The small flame kernel displaces from the spark plug and changes the distance to the furthest part of the cylinder wall. The burn duration increases if the flame moves toward the nearest wall of the cylinder (right) or decreases if it moves towards the center (left).**

Large-scale turbulent flow causes the flame kernel to move in a random walk from the spark plug. Keck et al. considered this the major cause of cycle-to-cycle variations in burn duration during the fast flame propagation stage [9]. Based on previous work by Beretta et al., it was shown that the distance that the flame center moved was significant. In their tests, the flame center moved about 14mm in quiescent conditions. Given a bore of 101.6mm of their engine, this distance significantly changes the effective starting point of combustion. Also, they noted that in their experiment, there was a critical flame radius r_f where the flame center stabilized. At $r_f =$ 28mm, it was clear in their experiment that the flame continued to move even as the envelope was quite large [10].

Bianco et al. continued research on this topic. They optically studied the flame shape at about the 0-2% burn mass angle under quiescent conditions as well as under swirl and tumble flows. Aside from burn duration effects, they noticed a distinct difference in mean expansion speed during the flame development stage between cycles where the kernel moved near the wall versus those where the kernel moved near the center of the combustion chamber [11]. Not only does the flame have a shorter distance to travel if it moves towards the center of the cylinder, but it also traverses this distance faster. Variations in location cause variations in burn duration from both of these effects.

Adding more understanding to the subject, Russ et al. measured the time for the flame to reach different points on the wall of the cylinder with ionization probes. They showed that when

they added mean flow vector to spark area in the cylinder, the resulting flame propagation would be uneven. It would take a shorter time for the flame to reach one side of the cylinder than the other, and the overall burn duration would increase [12].

2.1.3 Cold Surface Interactions

Aside from affecting the starting point of the outward flame propagation, the random walk of the flame kernel also varies the heat transfer with cold surfaces, most notably the side electrode of the spark plug. Modeled by Pischinger and Heywood, they found that a significant amount of energy is transferred to the electrode as heat if the flame does not move away from the center of the spark plug, as depicted in

Figure 2-2.

Faster Burn   Slower Burn
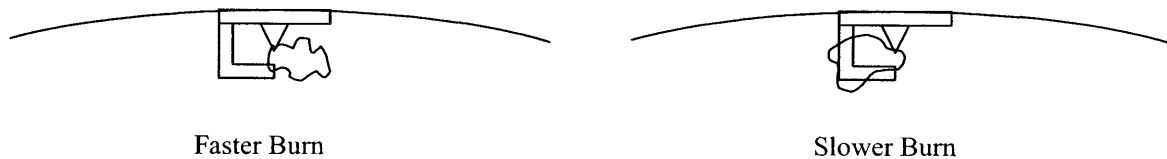
Figure 2-2   **Flame Kernel Development with Respect to the Spark Plug Electrodes. A significant amount of energy is transferred to the side electrode if the kernel stays between the electrodes (right).**

If the flame kernel does move out from between the electrodes, less energy is lost, and the expansion velocity is considerably higher. More energy is delivered to the flame kernel from the discharge positive column, as well. The heat loss was found to be comparable to the amount of energy released by the kernel from inception until it becomes 1.5mm in diameter, so it is significant. They further showed that given a reasonable amount of in-cylinder turbulence, the amount of heat transfer to the spark plug would change significantly cycle-by-cycle because of the random movement of the flame kernel [13].

If the mean flow in the vicinity of the spark plug is large compared to the turbulence, the randomness of the kernel movement will decrease. However, if the mean velocity is too high, the flow can quench the flame entirely. In a separate paper, Pischinger and Heywood suggest 3-5m/s as an optimal mean flow range to decrease random walk effects and to keep the flame from losing energy to the spark plug [14].

2.1.4 Turbulence Effects During Flame Propagation

Large-scale mean velocity fluctuations play an important role in variations in the flame propagation. The higher frequency velocity fluctuations distort the flame surface and affect the entrainment of the unburned mixture into the flame front. Each of these effects is on a cycle-by-cycle basis by variations. Wrinkling and folding the flame surface directly affects flame speed because it increases the frontal area of the flame. While the contribution to NIMEP CCV from the flame propagation stage is not negligible, it is smaller than the flame development stage because the flame propagates much faster when it is larger. Also, the flame surface is much larger so local fluctuations in burn rate become an increasingly small contribution to the burn rate averaged across the whole flame front.

2.2 Turbulent Intensity Fluctuations

The turbulent intensity, defined in Appendix A, represents the amount of small-scale turbulence in the cylinder. Small-scale turbulence viscous effects are generated by large-scale motion during the intake event. During the compression stroke, shear forces in the mixture dissipate the turbulence, reducing its level significantly from its maximum point during the intake stroke. Any CCV in large-scale fluid motion translate into variations in the level of small-scale turbulence, as well. Small-scale turbulence acts to entrain unburned mixture into the flame and to distort the flame shape, which increases the frontal area of the flame [5].

2.2.1 Laminar and Turbulent Contributions During Early Flame Development

The flame starts as a smooth, thin reaction zone where laminar effects dominate over turbulent ones. Turbulent eddies do not affect the flame speed until the flame becomes as large as the characteristic length scale of the eddies; however, this happens early, within the first 2% of the burn duration. Heywood notes that the laminar flame thickness of these sheets is on the order of 0.1mm whereas the turbulent wrinkles that occur are on the order of 1mm [5]. Bianco et al. used a spark-plug-fiber-optics probe to observe flame kernel behavior at 2% mass burned, and in their quiescent flow test, they found that the observed mean expansion speed was 40-50% higher than the calculated laminar mean expansion speed [11]. While turbulent effects are not negligible, they are much smaller here than during the flame propagation stage. Also, during this period they grow in influence. Equation 2-2, proposed by Beretta et al. [10], models the rate of flame propagation and shows the contribution of laminar and turbulent effects.

$$\frac{dm_b}{dt} = \rho_u A_f S_L + \frac{\mu}{\tau_b} \qquad (2\text{-}2)$$

dm_b/dt is the mass burn rate. ρ_u is the unburned charge density; A_f is the frontal area of the flame S_L is the laminar flame speed. τ_b is the turbulent time scale, and μ is a parametric mass, interpreted as the unburned mass entrained in the flame, as in Equation 2-3.

$$\mu = m_e - m_b = \rho_u l_T \left(A_L - A_f \right) \qquad (2\text{-}3)$$

Here, m_e is the total mass entrained in the flame, and m_b is the burned mass entrained in the flame. l_T is a characteristic length scale of wrinkles in the flame, and A_L is the laminar flame front area. The first component of the right side of Equation 2-2 represents the laminar propagation whereas the second component represents the burning of unburned mass entrained in the flame from turbulent wrinkling as illustrated in Figure 2-3.
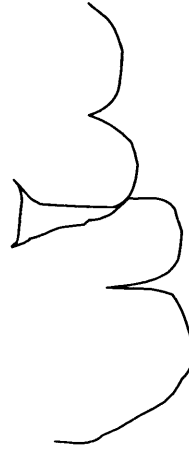
Figure 2-3   Flame Surface Detail. Turbulence causes wrinkling in the flame surface that entrains unburned charge into the flame.

Because turbulent eddies do not affect the flame when it is very small, the flame surface stays smooth and very little unburned charge becomes entrained in the flame. The second term in Equation 2-2 is small initially but its magnitude grows as the size of the flame grows. The flame grows comparatively slowly, initially because the first term is also small because the frontal area of the flame A_f is small. This is both because little mass becomes entrained in the flame and because the flame has not distorted from a spherical shape yet. The surface is smooth so A_f is approximately A_L, the laminar flame frontal area. Because of the slow propagation, the 0-2% burn duration can take approximately 30% of the total burn duration [11].

As the flame kernel grows, it reaches a critical size where it is the same length scale as the turbulent eddies in the charge. At this point, the flame front begins to fold and wrinkle, and

20

unburned mass begins to become entrained in the flame. Once this begins, the flame speed increases dramatically. Smith showed that this turbulent length scale is the Taylor microscale τ_M, defined by relating the fluctuating strain rate of the turbulent flow field $\partial u/\partial x$ to the turbulent intensity u', as in Equation 2-4 [15,5].

$$\frac{\partial u}{\partial x} \approx \frac{u'}{l_M} \tag{2-4}$$

l_M is the Taylor micro length scale, related to the Taylor micro time scale by Equation 2-5 in homogenous and isotropic turbulence, turbulence with no spatial gradients or preferred direction.

$$l_M = \overline{U} \tau_M \tag{2-5}$$

$\overline{U}$ is the average mean velocity.

A significant source of cycle-by-cycle IMEP variations can arise from CCV of this length scale. When the local turbulent intensity is higher, the Taylor micro length scale is smaller, and turbulence begins to play a significant role in burn rate earlier in the flame development process. Since the level of small-scale turbulence in-cylinder is caused by bulk motion, variations in bulk motion from cycle-to-cycle will generate global variations in small scale-turbulence.

Hill showed that there are indeed significant cycle-to-cycle variations in the mass fraction burn rate at the very beginning of combustion. From experimental data, he related the Taylor micro length scale to the burn duration standard deviation, as in Equation 2-6.

$$\sigma_0 = \frac{1}{2}\left(\frac{l_M}{4S_L}\right) \tag{2-6}$$

σ_0 is the standard deviation of his data. From this relationship, Hill showed that micro scale turbulence affects burn duration CCV through its magnitude in addition to its CCV [8].

Retarding or advancing the point at which turbulent flame propagation dominates over laminar propagation also has a secondary effect of timing this point with a decreasing turbulent intensity. Beginning at the intake event, the turbulent intensity consistently decreases through the compression stroke. When the transition to turbulence-dominated propagation is delayed, not only is a smaller portion of the flame propagation dominated by turbulence, but also the turbulence in-cylinder is weaker [5]. This provides a significant source for the variation of burn duration.

2.2.2 Flame Stretch

During the early part of the flame development stage, a phenomenon called flame stretch occurs where small-scale turbulence, on the order of the Taylor micro length scale, can cause the flame to stretch, thus increasing its frontal area. The flame strains normal to its gradient of heat and active species flux; the process results in lowered temperature and speed. Hacohen et al. conducted an experiment and a theoretical model to show that the flame stretch rate crucially affects early flame development and propagation rate later. Since the phenomenon is caused by small-scale turbulence, it is a mechanism of CCV [16].

2.3 Mixture Concentration Variations

Combined with fluid motion, variance of the mixture in the cylinder causes cycle-by-cycle variations in two distinct ways. First, the global mixture composition changes cycle-by-cycle. Next, the local composition changes. When considering the flame development stage, the effects of each one can be indistinguishable since the flame is only present in one spot.

2.3.1 Variations in Mixture Inhomogeneity

Considering local variations, turbulent fluid motion plays an important role in moving the developing flame kernel to regions of varying concentrations of fuel, air, and residual gas or moving varying concentrations of the mixture into the developing flame. CCV of the large-scale fluid motion can affect the contribution of mixture inhomogeneity to cycle-to-cycle fluctuations in burn duration. Mixture inhomogeneity affects flame propagation because it changes the local air-fuel ratio (AFR) as well as the dilution ratio from residual gas. Dilution ratio is defined as the mass of diluent divided by the total mass of mixture, as in Equation 2-7.

$$r_d = \frac{m_{diluent}}{m_{total}} \qquad (2\text{-}7)$$

At the smallest level, the flame propagates at the laminar flame speed, which is driven by the local composition of the mixture. Lee and Foster found that variations in local mixture composition near the spark plug affected IMEP only when the A/F was globally lean [17].

2.3.2 Global Mixture Variations

While variances of local mixture concentrations will average across the large flame frontal area, thus having negligible effects, global fluctuations by cycle result in noticeable

change in the dilution ratio. Sher and Keck considered this in terms of a fluctuation of volumetric efficiency η_v, defined as the mass of air that enters the chamber m_a divided by the displaced cylinder volume V_d times the intake air density $\rho_{a,i}$, as in Equation 2-8. So, it can be considered in terms of mass of residual gas as in Equation 2-9.

$$\eta_v = \frac{m_a}{\rho_{a,i} V_d} \tag{2-8}$$

$$\eta_v = 1 - \frac{m_{residual}}{m_a + m_{residual} + m_{fuel}} \tag{2-9}$$

They found that a fluctuation in the volumetric efficiency of 5% led to a change in burning velocity of 13%, which would noticeably affect NIMEP [18].

Hinze and Cheng used a global mixture perturbation method to understand the relative contributions that variations in air, fuel, and residual masses would have upon COV of GIMEP. They attributed 33% to fluctuations in residual gas mass, 7.5% to changes in air mass, and 4.6% to fluctuations in fuel mass. The remaining 54% was attributed to flow field and charge inhomogeneity effects [1].

2.4 Factors Influencing Cycle-to-Cycle Variation

Aside from those phenomena that cause cycle-by-cycle variations in burn rate and consequently, IMEP, there are also several factors that increase the likelihood of CCV indirectly through the flame speed. Decreasing the burn rate increases CCV, and increasing the burn rate reduces CCV. A faster burn reduces cycle-to-cycle variations because there is less time for random fluctuations in turbulence to alter the flame's trajectory. The flame kernel's movement from the spark plug would be reduced because it would reach the critical diameter where it stops moving sooner. Consequently, the variations of its movement would be lower. Some major factors that affect flame speed and the likelihood of CCV are fuel type, air-fuel ratio, dilution ratio, engine load, spark timing, large-scale fluid motion, and engine speed.

2.4.1 Mixture Effects

The mixture defines the laminar flame speed, so changing the air-fuel ratio, the dilution ratio, or the type of fuel will change the laminar flame speed. The laminar flame speed is a strong function of the adiabatic flame temperature, which can be found from an enthalpy balance as shown in Equations 2-10 and 2-11.

$$\Delta H_{products} - \Delta H_{reactants} = 0 \qquad (2\text{-}10)$$

$$\left(h_{formation} + \int_{T_0}^{T} c_p(T)dT \right)_{Reactants} = \left(h_{formation} + \int_{T_0}^{T} c_p(T)dT \right)_{Products} \qquad (2\text{-}111)$$

ΔH is the enthalpy difference from a reference enthalpy. $h_{formation}$ is the specific enthalpy of formation of each specie. c_p is the specific heat capacity. If more diluent is added to the mixture, the mixture's thermal mass increases, and the adiabatic flame temperature will decrease. If the air-fuel ratio is changed, the laminar flame speed will change, as well. The equivalence ratio at which the maximum flame speed occurs depends on the fuel [3]. The fuel type matters because it will change the enthalpy of formation of the fuel as well as the stoichiometry.

Another way to vary the laminar burn rate is to vary the load. Temperatures are higher at higher loads because of the smaller heat loss relative to the charge energy. Turbulence levels are also higher due to more mass flow through the intake valves [5].

2.4.2 Turbulence Effects

Changing the level of turbulence in cylinder can also significantly change the burn rate. First, the size of the first eddy to interact with the flame kernel is important because it determines when turbulence will accelerate flame propagation. Also, the level of turbulence in-cylinder will determine the rate of mass entrainment into the flame front. As mentioned earlier, a mean velocity in the vicinity of the spark plug will cause the flame kernel to move away from the spark plug to grow faster. Also, the direction in which the kernel is moved will either shorten or lengthen the burn duration depending on whether the kernel is moved toward the center of the cylinder or away from it.

2.4.3 Inducing Turbulence

The amount of turbulence in-cylinder depends on the geometry and velocity of the air flow inducted through the intake valves and on the geometry of the combustion chamber. Up to a point, raising the engine speed, for example, causes air to rush into the cylinder at a higher velocity, which increases in-cylinder turbulence. Engine designers also employ strategies to generate high velocity airflow into the cylinder in such a way as to generate a particular flow in the cylinder.

One strategy is to generate swirl, a rotational fluid motion about the axis of the cylinder. Generated during the intake stroke, about a quarter to a third of the initial rotational momentum

is dissipated as heat to the walls and through shear in the fluid by the end of the compression stroke. However, a squish strategy can also be employed to increase fluid velocity during compression. If the piston features a bowl, the rotating mass will be forced towards the axis of the cylinder by this bowl geometry during compression, and by conservation of angular momentum, the rotational speed of the fluid will increase. Since the rotation will be stronger near the piston than near the head, the piston bowl matters more than a hemispherical head does [5]. During combustion, Witze notices two ways swirl effects flame propagation. First, light swirl generates a higher level of in-cylinder turbulence to aid flame propagation through diffusion. If the spark plug is located in the path of the rotating flow, strong swirl will accelerate the burn rate through a convective process [19].

A second strategy for developing flow in-cylinder is to induce a tumbling motion, a rotation about an axis perpendicular to the cylinder axis, during intake. Unlike in the swirl strategy, the compression stroke significantly changes the geometry in which the tumbling is occurring, and consequently, tumbling breaks down before top center. What results is a high level of turbulence near the spark plug, if it is located near the center of the head. A notable feature of tumble is that it affects the flame kernel differently depending on ignition timing. If ignition is early, the spark may witness a strong mean flow; whereas, if ignition is significantly retarded, only a high level of turbulence will affect the kernel [3].

Chapter 3 Experimental Method

The methodology used to study combustion stability was to induce additional turbulence to the charge motion in one set of tests and to change the laminar flame speed of the mixture in a second set, varying the spark timing in both. First, combustion tests were conducted in which the ratio of airflow through an added air jet versus through the manifold was varied to study the effects on COV of NIMEP and on burn duration. Also, combustion tests were conducted in which nitrogen in air was substituted with argon or carbon dioxide to delineate the effects of laminar versus turbulent flame properties on burn rate and COV. Each of these sets of tests was conducted at operating conditions used during fast idle.

3.1 Combustion Test Experimental Procedure

The first series of tests conducted was a baseline in which the speed, load, AFR, and coolant temperature were held constant as spark timing was varied. No air jet was used in these tests, and gaseous propane was introduced into the intake airflow in the middle of the runner. The in-cylinder pressure trace, manifold air pressure (MAP), manifold air mass flow, and the exhaust temperature were recorded for each test. Approximately 320 cycles were recorded.

3.1.1 Experimental Parameters

In these tests, as in each of the other combustion tests, the engine was run at an operating condition to approximate a fast idle condition. Engine speed was held at 1400rpm. The load was kept at 2.6bar NIMEP, which corresponds to approximately 20 Nm for a four-cylinder engine, and coolant temperature was kept at 20°C. Spark timing was varied from 20 crank angle degrees (CAD) before top center (BTC) to 20 CAD after top center (-20 CAD BTC). For consistency, all spark timing will be referred to as before top center. The error of each parameter is noted in Table 3-1.

Parameter	Value	Error Bound
Speed	1400 RPM	± 8 RPM
NIMEP	2.6 bar	± 0.1 bar
Coolant Temperature	20°C	± 1.5°C
Relative AFR (average)	1.000	± 0.005

Table 3-1 **Operating Parameters Held Constant with Associated Bounds.**

3.1.2 Air Jet Tests

Next, two sets of combustion tests were conducted to see the effects that additional charge motion would have on combustion stability, burn duration, and exhaust temperature. The air jet was designed to induce swirl motion in one set of tests and tumble motion in the other set. At each spark timing, the ratio of intake air from the jet versus from the intake manifold was varied from 0 to 1. The in-cylinder pressure trace, manifold pressure trace, exhaust temperature, and the manifold air mass flow were recorded.

3.1.3 Laminar Flame Speed Tests

The composition of inert gas in the mixture was varied in two sets of tests to differentiate laminar and turbulent effects on burn duration and COV of NIMEP. In one set, intake air partially was replaced by O_2 and Ar to increase laminar flame speed. In the other set, the intake air was partially replaced by O_2 and CO_2 to decrease laminar flame speed. In these tests, load was kept at 2.6 bar NIMEP. The amount of argon or CO_2, depending on the test, was introduced equivalent to the mass of replaced nitrogen. The swirl air jet was left installed in the intake port to allow for comparison between these tests and the air jet although no air was introduced through it.

3.2 Apparatus

The apparatus consisted of a 1.8L, four-cylinder Nissan spark ignition engine equipped to run on one cylinder. The engine's speed was maintained at a constant speed by a motoring dynamometer. The experiment was conducted at the Sloan Lab at MIT in Cambridge, MA.

3.2.1 Engine Specifications and Setup

A 2003 Nissan QG18DE engine was used. The specifications are shown in Table 3-2.

Displacement	$442.3 cm^3$
Compression Ratio	9.5
Bore	80mm
Stroke	88mm
Clearance Volume	$208.1 cm^3$
Connecting Rod Length	140.5mm
Valve Timing (held constant for tests)	IVO: 5° BTDC; IVC: 51° ABDC EVO: 26° BBDC; EVC: 2° BTDC

Table 3-2   Nissan GQ18DE Specifications.

The test engine featured a fast-burn combustion chamber. The chamber had a bowl in piston and a modest bowl in the chamber roof. The spark plug was centrally located, and the engine featured double overhead cam actuation of four valves per cylinder, as shown in Figure 3-1.
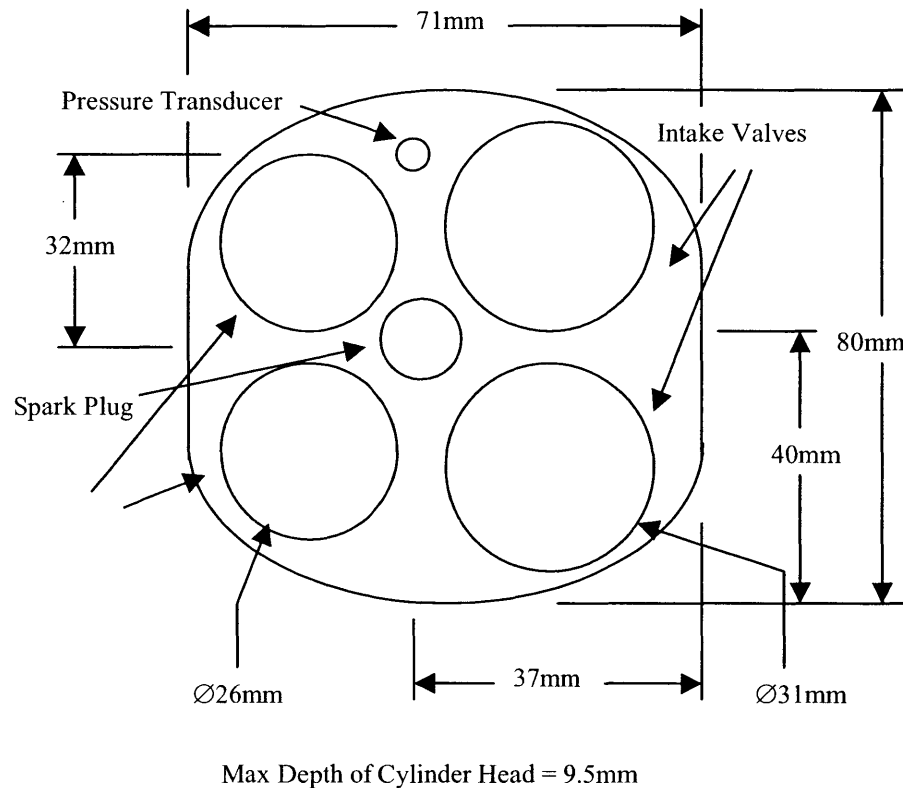
Figure 3-1   **Engine Cylinder Head Diagram. The engine head is a shallow hemisphere design with four valves and a near-centered spark plug.**

Also, the engine featured variable intake valve timing and charge motion plates between the intake runners and the ports. The valve timing was fixed in the default position as noted in Table 3-2, and charge motion plates were kept in the closed position.

The engine was modified for single-cylinder operation. The intake and exhaust of the test cylinder were isolated from those of the other three cylinders. A plate was installed between pieces of the intake manifold to block air flow from the throttle to the three motored cylinders. Small air filters were added to the runners of these cylinders to allow air to enter them to reduce the resistance upon the dynamometer caused by pumping air through them. The exhaust manifold was modified to keep the test cylinder's exhaust isolated through the entire exhaust system. Throughout all tests, the dummy cylinders were motored.

3.2.2 Dynamometer

A 3DSE Dynamatic Co. dynamometer controlled the speed of the engine and absorbed its power output. The 40hp dynamometer featured an effective speed range of 900rpm to 3500rpm. The engine's crankshaft was directly coupled to the dynamometer with a flexible coupling. While the dynamometer measured the brake torque of the engine, the measurement was not accurate enough to be useful.

3.2.3 Engine Temperature

The target coolant temperature for testing was 20°C. The coolant temperature was measured by K-type thermocouples at the inlet and the outlet of the coolant from the engine. The average of these two temperatures was kept at 20°C ± 1.5°C. A VWR 1179PD, 1hp chiller was used to dissipate the heat load of the engine. The chiller was rated to dissipate 2850W of energy at 20°C.

3.2.4 Intake System and Charge Motion Jet

The experiment mainly focused on modifying the intake system and how it affected combustion. In the baseline case, the air flowing through the custom throttle was directed completely to the test cylinder. The throttle consisted of a large ball valve and a fine globe valve. Adjustments were made by hand. Upstream of the throttle was a 55-gallon dampening tank and then the mass flow meter. The mass flow meter was a 505-9A-02 made by Kurz Instrument Inc. It was rated for 0-23.6g/s, and the meter's output varied by ± 0.02g/s at most during steady-state operation. The manifold air pressure was measured by a Model SA pressure transducer made by Data Instruments, which is now owned by Honeywell. The MAP sensor was mounted in the plenum of the manifold. Its range was 0-25psia.

The charge motion jet was a 1/4in. copper tube with an inside diameter of 0.190in. The jet was supplied by a pressurized bottle of air, and the flow was regulated by a pressure regulator and an orifice of known diameter that was changed for different flow rates. The jet was mounted through the fuel injector hole through the port so that the end of the tube was positioned just behind an intake valve, a shown in Figure 3-2. The jet was directed in two positions to generate swirl motion and tumble motion respectively, also shown in Figure 3-2.
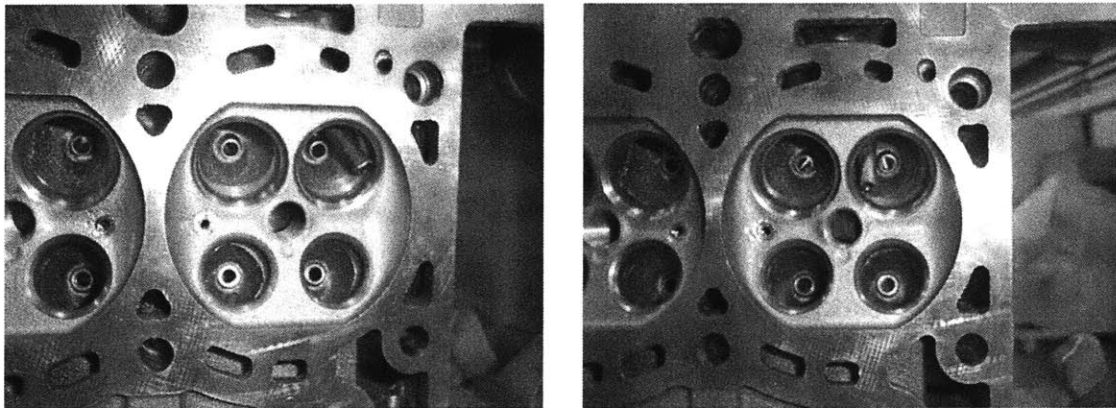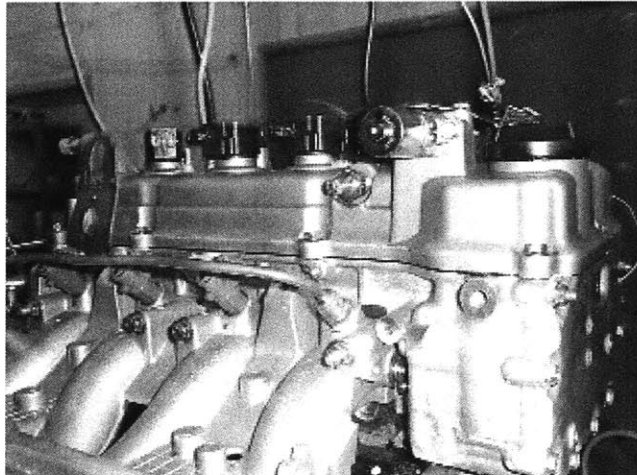
Figure 3-2   **Charge Motion Jets. The charge motion jet was installed immediately behind an intake valve to generate swirl (bottom left) or tumble (bottom right). The jet was mounted through the fuel injector hole (top).**

For the laminar burn duration tests, oxygen and argon or carbon dioxide were introduced separately from pressurized bottles into the flow upstream of manifold. A pressure regulator and an orifice of appropriate area regulated the flow of each gas.

3.2.5 Fuel

In all combustion tests, gaseous propane was used as a fuel. Propane was chosen instead of a liquid fuel because it is gaseous. Cycle-by-cycle variations in liquid-fuel vaporization would contribute to cycle-by-cycle torque variations. Also, the addition of the air jet may have strongly affected fuel vaporization.

In each combustion test, the propane was introduced at a constant rate into the intake system, and the flow was controlled by hand with a needle valve. In the baseline configuration, the propane was introduced into the middle of the intake runner. This was adequate while a

30

substantial portion of the flow passed through the runner. However, when most of the air passed through the jet, mixing problems arose, as variation in the AFR significantly increased. To address this issue, a small fuel tube was installed in the runner and in the port to introduce fuel next to the air tube.

The amount of fuel consumed could be estimated using the air mass flow with the relative air-fuel ratio. The equivalence ratio was kept at 1.000 ± 0.005, although it deviated by $\pm$ 0.005 during steady-state operation. The relative air-fuel ratio was measured by a Nissan wide-band O_2 sensor and an ETAS Lambda Meter.

3.2.6 In-Cylinder Pressure Measurements

In-cylinder pressure measurements were necessary to determining the COV of NIMEP as well as to correctly set the engine to the proper operating condition. A Kistler 6051A piezoelectric pressure transducer was mounted in the roof of the combustion chamber 32mm off center, as shown in Figure 3-1. The sensor signaled a charge difference to the Kistler 5010 Dual Mode Charge Amplifier through a high impedance cable. This type of sensor effectively senses changes in pressure; however, it does not accurately sense absolute pressure. A dead-weight pressure calibration device was used to establish the linearity of the pressure measurement system. The absolute pressure in-cylinder was found by recording both the in-cylinder pressure signal and the MAP. The in-cylinder pressure was pegged to the manifold pressure at BC before the compression stroke. The in-cylinder pressure was calibrated against the manifold pressure for every cycle to correct against any signal drift possibly caused by charge accumulation in the piezoelectric transducer system.

3.2.7 Data Acquisition System

The data acquisition system consisted of several analog signals recorded by hand and the quickly changing analogue signals that were recorded by the computer. Exhaust temperature, intake air temperature, coolant inlet temperature, coolant outlet temperature, mass airflow through the manifold, and engine speed were all recorded by hand. To record in-cylinder pressure and manifold pressure, a National Instruments data acquisition system was used with a desktop computer. Specifically, a BNC 2090 board was used in conjunction with a PCI-6025E card. Labview was used to record data and to calculate NIMEP real-time. An encoder mounted on the end of the crankshaft was used to provide a signal on 360 points per revolution on one

channel and one point per revolution on a different channel. Every other signal of this second channel was ignored, and the remaining one was aligned with BC before the compression stroke. The 360-point signal was used as a clock signal for data acquisition, and the BC signal was used as a trigger. This BC signal was also superimposed over the in-cylinder pressure trace as a reference point for data analysis. The encoder was an H25E-F18-SS-360-ABZ-740GR-LED-SM16-S made by BEI Motion Systems Inc.

3.2.8 Engine Control System

All tests were conducted during steady-state operation so a manual control system was adequate. The throttle and the fuel flow valve were adjusted by hand to keep the mixture at a stoichiometric ratio. The NIMEP calculation done by Labview was used to check that the engine load was correct.

Chapter 4 Results and Discussion

To understand the dependence on COV of laminar flame speed and turbulence, four sets of combustion tests were conducted. In two sets of turbulence tests, an air jet was installed behind one of the intake valves to increase in-cylinder turbulence, and pressure data were taken for nine spark-timing settings from 20° BTC to 20° ATC (referred to as –20° BTC). One spark sweep at varying jet flows was done for each of two jet orientations, which were designed to generate swirl and tumble, respectively. In the two sets of laminar flame speed tests, nitrogen was replaced with carbon dioxide or argon to reduce or increase laminar flame speed, respectively. The presented data consist of COV of NIMEP, burn duration, combustion phasing, and exhaust temperature with respect to jet flow, spark timing, relative laminar flame speed, and one another. All tests are taken at 20°C average coolant temperature, an equivalence ratio of 1.00, 1400rpm, and 2.6bar NIMEP. For comparison, a baseline is presented first.

4.1 Baseline

Exhaust temperature, COV of NIMEP, and 0-10%, 0-50%, and 10-90% burn durations were collected for a spark timing sweep from 20° BTC to –20° BTC. In this set of data, the swirl jet is installed in the intake port but not used. The presence of the 1/4 in. copper tube may affect the airflow into the engine, so it is installed for a more accurate comparison.

4.1.1 Baseline Exhaust Temperature

As shown in Figure 4-1, the exhaust temperature is 463°C when the timing is set to 20° BTC. The exhaust temperature consistently rises as timing is retarded, reaching 648°C at –20° BTC. This affirms the claim that retarding the spark timing during start-up will accelerate catalyst light-off by heating the exhaust.

4.1.2 Baseline COV and Burn Durations

The COV of NIMEP and the 0-10%, 0-50%, and 10-90% burn durations are plotted together in Figure 4-2. COV reaches a minimum of 3.85% at a spark timing of 15° BTC, indicating that this is the closest point to maximum brake torque (MBT) timing. COV increases with a positive derivative as spark timing is retarded from this point, reaching 6.27% at –5° BTC and 9.55% at –20° BTC.

Each of the three burn durations plotted remains approximately flat between the timing of 20° BTC and 10° BTC. Then, as timing is retarded, the burn rates increase consistently. From the minimum value to the maximum values, the 10-90% burn duration is lengthened the most, about 88%. The 0-10% burn duration increases by 80%, and the 0-50% burn duration increases by 69%. Presumably, the longer combustion period allows turbulent fluctuations to cause more variability between cycles. The 0-50% duration and the 10-90% duration should show similar behavior to the 0-10% behavior because the early flame development affects flame propagation speed. Since turbulent intensity is highly dependent on combustion phasing, the speed of early flame development will determine the turbulent intensity during the propagation stage of the burn [3].

4.2 Turbulence Tests

For the turbulence tests, the jet flow rate was adjusted from no flow to the entire flow or close to it. The airflow through the manifold was adjusted to keep the engine load constant at 2.6bar NIMEP. Each jet was mounted as shown in Figure 3-2.

4.2.1 Exhaust Temperature Change

If the addition of a turbulence-enhancement strategy is considered for fast catalyst light-off, it is necessary to see how additional turbulence affects the exhaust temperature. The change in exhaust temperature with jet flow is examined in Figure 4-3 for the swirl jet and in Figure 4-4 for the tumble jet. Except for a datum at −5° BTC in the swirl jet set, the exhaust temperature remains within 5% of the baseline set for each test.

4.2.2 Swirl Jet COV of NIMEP

In Figure 4-5, COV of NIMEP is plotted against jet flow, normalized against the total airflow. As is consistent with the baseline, more retarded spark timings feature higher overall COV percentages. The swirl jet is effective at reducing COV approximately 30% at each spark timing at various flow rates, as shown in Table 4-1.

In each of the spark timing sets at 5° BTC and at more retarded timings, COV decreases with increased jet flow until a point where it markedly increases. These data are replotted in Figure 4-6 to show that this point occurs approximately at 1.1 g/s in each of the sets where it occurs. In several cases, this point is the minimum COV of the set. After a peak in some of the

curves, the COV again falls as jet flow is increased. Witze found similar results in his 1982 study. Comparing his COV data with his photographs, he concluded that when the jet flow was low, the flame propagation was driven by the turbulent diffusion process. The jet added turbulence and enhanced entrainment velocity. If the jet flow was increased enough, there was an additional turbulence generating mechanism due to the wake formed by the jet-spark plug interaction. He called this convection induced flame enhancement. At the transition between the diffusion and convection mechansims, COV notably increased, but once the jet strength was increased enough, the convection propagation became consistent and COV dropped [19].

Spark Timing	Baseline COV	Min. COV	COV Decrease	Jet/Total Flow at Min. COV	Jet Mass Flow at Min. COV (g/s)
20°	4.26%	2.86%	33%	0.83	0.95
15°	3.85%	2.69%	30%	0.74	0.95
10°	4.01%	2.74%	32%	0.73	0.95
5°	4.43%	3.05%	32%	0.48	0.64
0°	5.37%	3.59%	33%	0.92	1.32
-5°	6.27%	4.05%	35%	0.28	0.4
-10°	7.26%	4.63%	36%	0.58	1.04
-15°	8.86%	5.83%	34%	0.48	0.97
-20°	9.55	6.88	28%	1.0	2.39

Table 4-1   Swirl Jet Improvements to COV.

4.2.3 Swirl Jet Burn Durations

For the swirl jet tests, the 0-10%, 0-50%, and 10-90% burn durations are plotted against normalized jet flow in Figure 4-7, Figure 4-8, and Figure 4-9, respectively. The 0-10% burn duration shows a decrease as jet flow is increased at low jet flows, but it reaches a minimum or levels off near 0.6 in most cases. The 0-50% burn duration plot shows similar trends. The 10-90% burn duration plot weakly shows this trend of decreasing duration as jet flow increases at low jet flows. The effect is more pronounced during the first 10% of the burn.

4.2.4 Tumble Jet COV of NIMEP

As shown in Figure 4-10, the tumble jet affects COV differently than the swirl jet does. The more advanced spark timings, 20° BTC and 15° BTC reach a minimum COV at low jet flow, 24% of total flow, and increase as jet flow is increased as shown in Table 4-2. The 10° BTC and 5° BTC timings feature a minimum COV at full jet flow. They decrease initially then flatten until the jet is increased to full flow. The tests taken at more retarded spark timings show a decrease in

COV as the jet is increased to approximately two thirds of the flow, about 80% for 0° BTC. However, increasing the jet flow past this point increases variability.

The earliest spark timings should witness a different flow than later ones, as the tumble motion should break down into turbulence by top center. 20° BTC and 15° BTC show a slight decrease at low jet flow because the flame kernel is probably feeling slightly stronger direct fluid motion caused by the jet. As the jet flow is increased, the flow exceeds optimal flow velocity range, and COV increases to a point higher than the baseline. The curves for later timings feature consistent reduction in COV with increased jet flow up to a higher amount than the earlier timings because the jet is likely directly increasing the level of turbulence rather than creating a significant mean flow that is interacting with the early flame kernel. At some turbulence level in each of these timings, COV increases. This may be due to decreased mixing quality.

Spark Timing	Baseline COV	Min. COV	COV Decrease	Jet/Total Flow at Min. COV	Jet Mass Flow at Min. COV (g/s)
20°	3.55%	3.19%	10.1%	0.24	0.31
15°	4.02%	3.27%	18.7%	0.24	0.31
10°	4.50%	3.13%	30.4%	1.00	1.36
5°	4.82%	2.72%	43.6%	1.00	1.36
0°	5.57%	3.31%	40.6%	0.81	1.21
-5°	6.31%	3.92%	37.9%	0.68	1.13
-10°	6.67%	4.27%	36.0%	0.67	1.21
-15°	7.45%	5.26%	29.4%	0.67	1.49
-20°	8.69%	7.19%	17.3%	0.55	1.36

Table 4-2   Tumble Jet Improvements to COV.

4.2.5 Tumble Jet Burn Durations

Shown in Figure 4-11, Figure 4-12, and Figure 4-13, the 0-10%, 0-50%, and 10-90% burn durations for the tumble jet tests each feature a decrease in burn duration as jet flow is increased. In the 0-10% and 0-50% plots, the curves of the earliest timing settings, 20° BTC, 15° BTC, 10° BTC, and 5° BTC feature consistent decline in burn duration as the jet is increased to full flow. The 10-90% plot shows 20° BTC and 15° BTC level off whereas 10° BTC increases at full jet flow and 5° BTC continues to decrease as jet flow is increased. Later spark timing curves show a decrease in burn duration with increased jet flow at low jet flows in each of the three plots. These curves either reach a shallow minimum between 0.4 and 0.7 and then rise slightly at high jet flows, or the flatten near a jet flow ratio of 0.5

4.3 Laminar Flame Speed Tests

In two sets of tests, replacing the nitrogen in air with a different inert gas varied the mixture's laminar flame speed. Argon was used to increase the laminar flame speed, and carbon dioxide was used to decrease it. The relative laminar flame speed for each mixture used was estimated with respect to that of a stoichiometric mixture comprised of air and fuel. See Appendix A for how it was calculated.

4.3.1 Laminar Flame Speed COV of NIMEP

As shown in Figure 4-14, COV increases as laminar flame speed is decreased. Along each spark timing curve, as laminar flame speed is decreased, COV increases approximately linearly until a point where is suddenly increases rapidly. This point appears to be between S_L/S_0 = 0.8 and 0.9 for all curves. The linear slope that the curves display tends to become more negative as the spark timing is more retarded. Also, when the laminar flame speed is very high the more retarded timings achieve a lower COV than the timings closer to the MBT point for the baseline mixture.

This behavior is explained by the decreasing turbulent intensity in-cylinder as spark timing is retarded. Turbulence dissipates, starting from the end of the intake event, with each successive move to a more retarded ignition time. So, there is a lower amount of turbulence at spark. This results in a larger first-eddy size, which allows more time for the growth of the flame kernel in a laminar-dominated regime. At normal, early ignition timings such as 15° BTC, the increase in laminar flame speed has almost no effect; whereas, at -10° BTC, for example, a much greater reduction in COV is realized. Also, at late spark timings, the reduced turbulence and increased laminar flame growth allows an improvement in COV beyond the baseline MBT value. At each spark timing later than the original MBT timing, 15° BTC, COV is reduced increasingly more below the MBT timing level. An explanation for this behavior is that the reduced turbulence of late spark timing results in a larger average eddy size interacting with the flame kernel. The interaction is later because the kernel must grow to the same length scale as the eddy. While under normal laminar flame speed conditions, the kernel would move far from the spark plug in this time, the kernel grows quickly and drifts little. Not only does the kernel avoid much of the random walk phenomenon, the laminar flame speed also grows the kernel quickly avoiding variations from flame stretch and small-scale turbulence that is less intense at late

timing. Compared to the effects of artificially increasing turbulence at late timing, it appears that the increased turbulence may have adverse effects on CCV that laminar flame speed enhancement does not cause.

4.3.2 Laminar Flame Speed Burn Duration Tests

The burn duration plots, shown in Figure 4-15, Figure 4-16, and Figure 4-17, feature similar trends as the COV plot for the laminar flame speed tests. In each spark timing curve, the burn durations in each plotted percentage increase linearly as laminar flame speed is decreased until a point at which the burn duration rises steeply. This point, between $S_L/S_0 = 0.8$ and 0.9 for each curve, corresponds to where the COV markedly increases. As in the COV plot, laminar flame speed enhancement affects the later timing curves noticeably more than the early timing curves. For example, in the 0-10% plot, the -20° BTC curve features 20° CAD difference between where the slope changes at low S_L/S_0 to the higher S_L/S_0. However, the 20° BTC curve only changes by 5° for this range.

4.4 Global Data

To examine the relationships between COV, exhaust temperature, and burn duration, all the data are shown together in several plots.

4.4.1 Exhaust Temperature vs. Combustion Phasing

To show the effect of combustion phasing on exhaust temperature, exhaust temperature is plotted against the crank angle at which 50% of the charge is burned (CA 50%), as shown in Figure 4-18. CA 50% is a useful metric to describe the phasing of combustion during the cycle because 50% of the mixture combusts at about half the time required for complete combustion. Exhaust temperature features a linear correlation with CA 50%. The conclusion that a later burn causes an increase in exhaust temperature is consistent with the explanation that there is less heat transfer to the cylinder walls if the burn is later. Also, a lower percentage of the chemical energy of the fuel is transferred to the piston as work at later combustion phasing so the burned gas is hotter at EVO, as a result.

4.4.2 Exhaust Temperature vs. COV

The exhaust temperature is plotted against COV for the turbulence data and the laminar flame speed change data as shown in Figure 4-19. There is a correlation between exhaust temperature and COV in the turbulence data. The laminar speed change data show a looser correlation. It is likely that this correlation is mostly caused by changing in combustion phasing. However, this laminar speed data is confounded by the fact that the charge thermodynamic properties are changed substantially. The relationship between exhaust temperature and combustion phasing is clear, as in Figure 4-18. Also, from Figure 4-3 and Figure 4-4, it is clear that the added turbulence does not affect exhaust temperature.

4.4.3 COV vs. Combustion Phasing

Figure 4-20, Figure 4-21, and Figure 4-22 show COV of NIMEP plotted against CA 50% CA 90% and CA 10%. All of the data are plotted in each of these figures, but the data from each set is distinguished to elucidate why the plot takes the shape it does. Considering the data from all tests, COV seems to have a weak correlation with combustion phasing, as shown in the CA 50% plot in Figure 4-20. COV increases, generally, as CA 50% increases. COV and combustion phasing correlate much better in the turbulence data than in the laminar flame speed data, especially when CA 50% is later than 190 CAD. While the tumble and swirl data seem to overlap each other, the CO_2 data features a higher COV than the argon data for all CA 50% points. They also diverge as CA 50% increases. The shapes of the CO_2 and the Ar data are different, as well. The CO_2 data seem to show a linear relationship, although the points are spread out. The argon COV data tend to be clumped where CA 50% is early and then spread out when CA 50% is later, thus showing less of a correlation.

In Figure 4-21 and in Figure 4-22, COV is plotted against CA 10% and CA 90%, respectively. In both of these plots, the turbulence data show the same behavior as in CA 50%; however, the laminar data show different behavior in each one. In the CA 10% plot, the Argon data are about the same as in the CA 50% plot, but the CO_2 data are more spread out. In the CA 90% plot, both the Argon and the CO_2 data fall more tightly around the line that the turbulent data form.

4.4.4 COV vs. Burn Duration

For the global data set, COV is plotted against 0-10%, 0-50%, and 10-90% burn duration in Figure 4-23, Figure 4-24, and Figure 4-25. In each plot, there appears to be a strong linear correlation between COV and burn duration or flame speed, inversely. As burn duration increases, COV increases. However, at the shortest burn durations in each range plotted, the linear relationship would project COV to drop below 2% as the 0-10% stage is reduced to 15 CAD. This point is at about 23 CAD for the 0-50% segment and 15 CAD for the 10-90% duration. There is considerable noise in the data at long burn durations in the 0-10% plot and the 10-90% plot. These points that do not align with others are related to the significant, non-linear increase that both COV and burn duration display as the laminar flame speed is reduced, shown in Figure 4-14 through Figure 4-17. The points in question lie at the point where the curves begin to deviate from their linear path to the non-linear one.
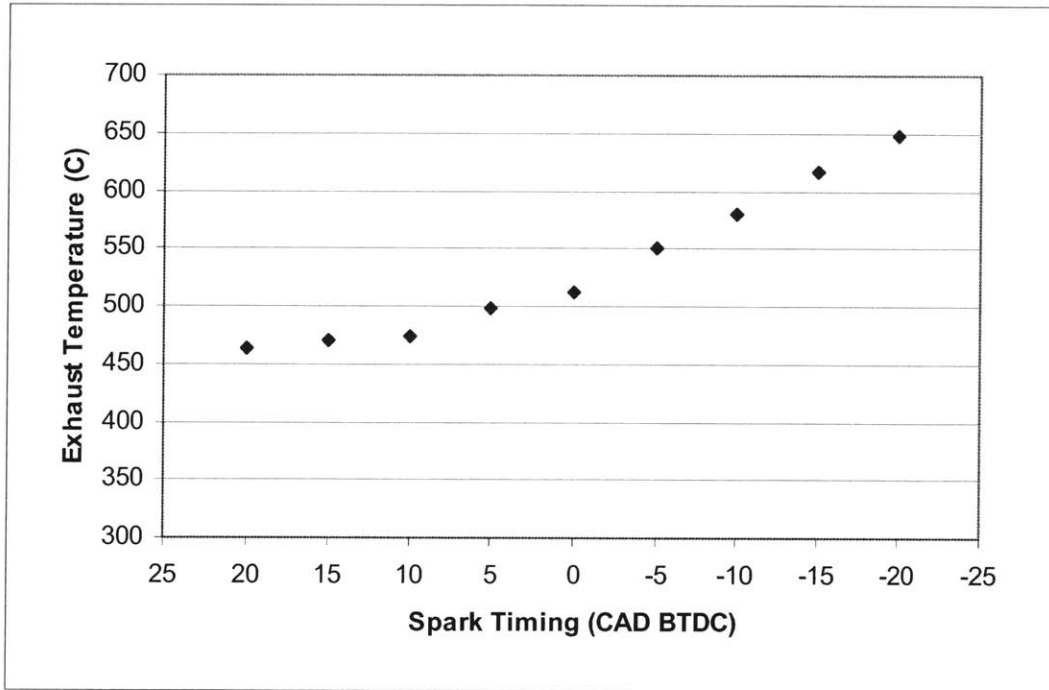
Figure 4-1   Baseline: Exhaust Temperature vs. Spark Timing. Exhaust Temperature is measured in the exhaust manifold 1 in. from the port exit. The swirl jet is installed but not used.
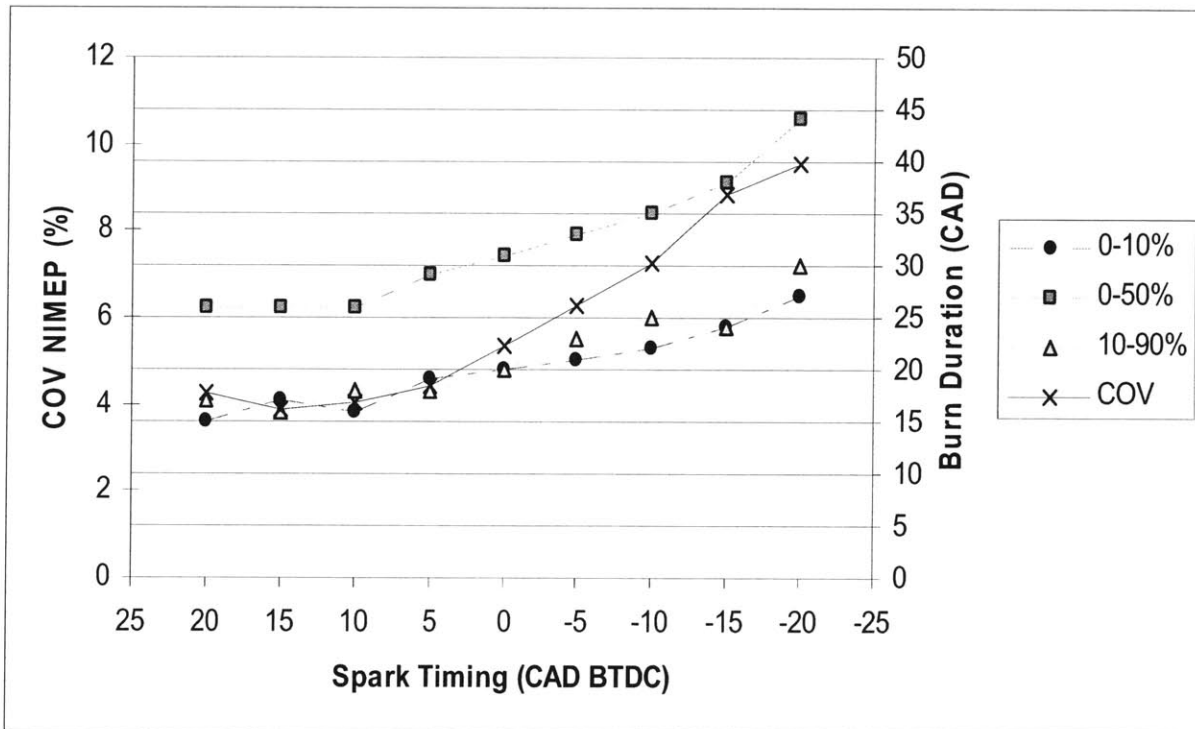
Figure 4-2   Baseline Burn Duration and COV NIMEP plotted against Spark Timing. The swirl jet is installed but not used.
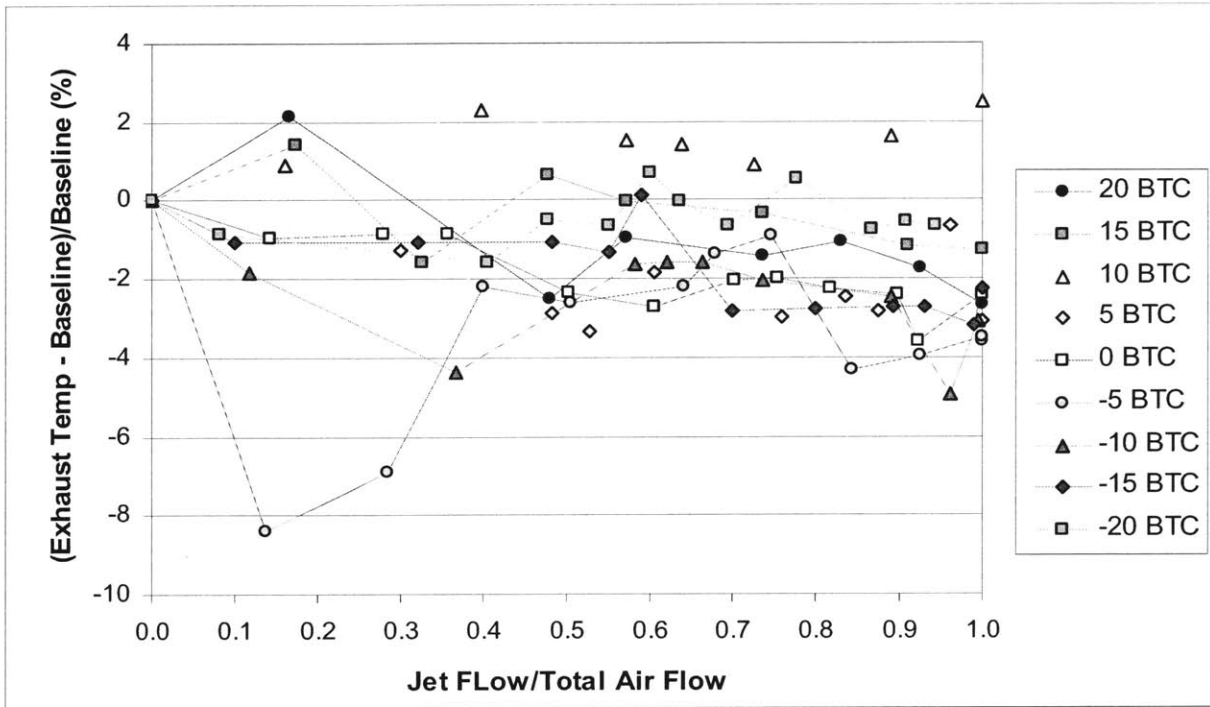
Figure 4-3   Difference in Exhaust Temperature from Baseline in Swirl Jet Tests. The difference in exhaust temperature from the baseline is plotted against jet flow, which is normalized against total airflow.
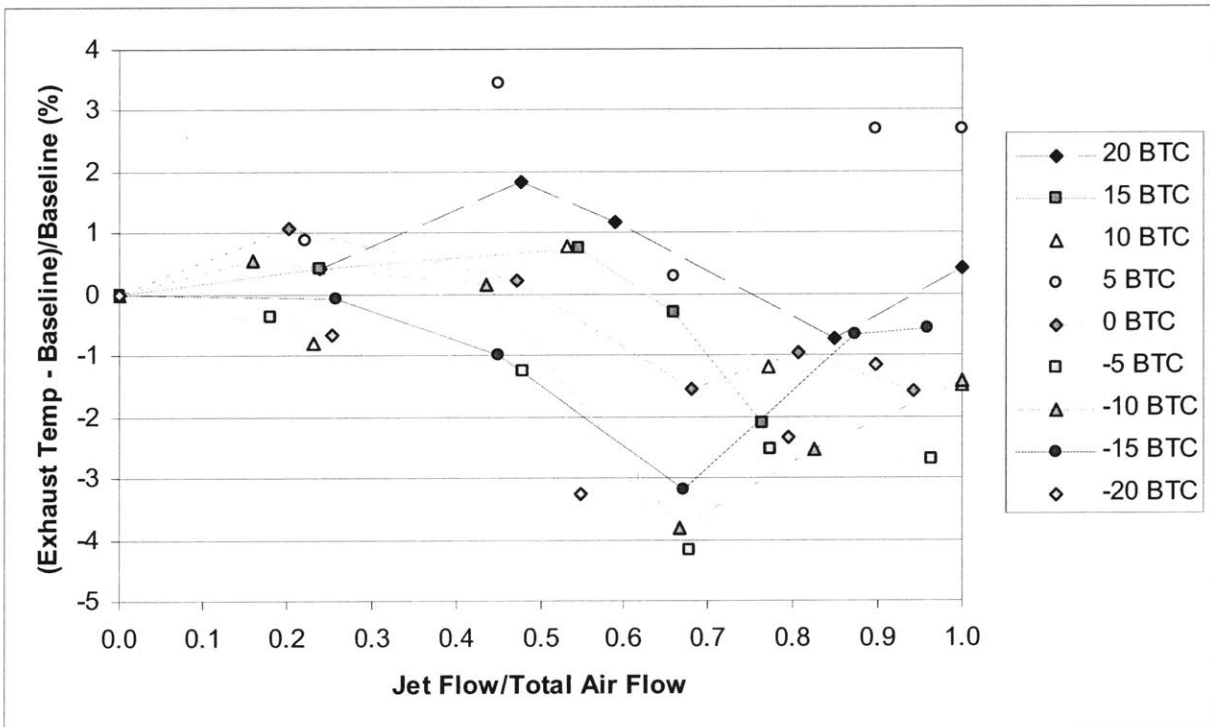
Figure 4-4   Tumble Jet: Exhaust Temperature Percent Change vs. Percentage Jet Flow.
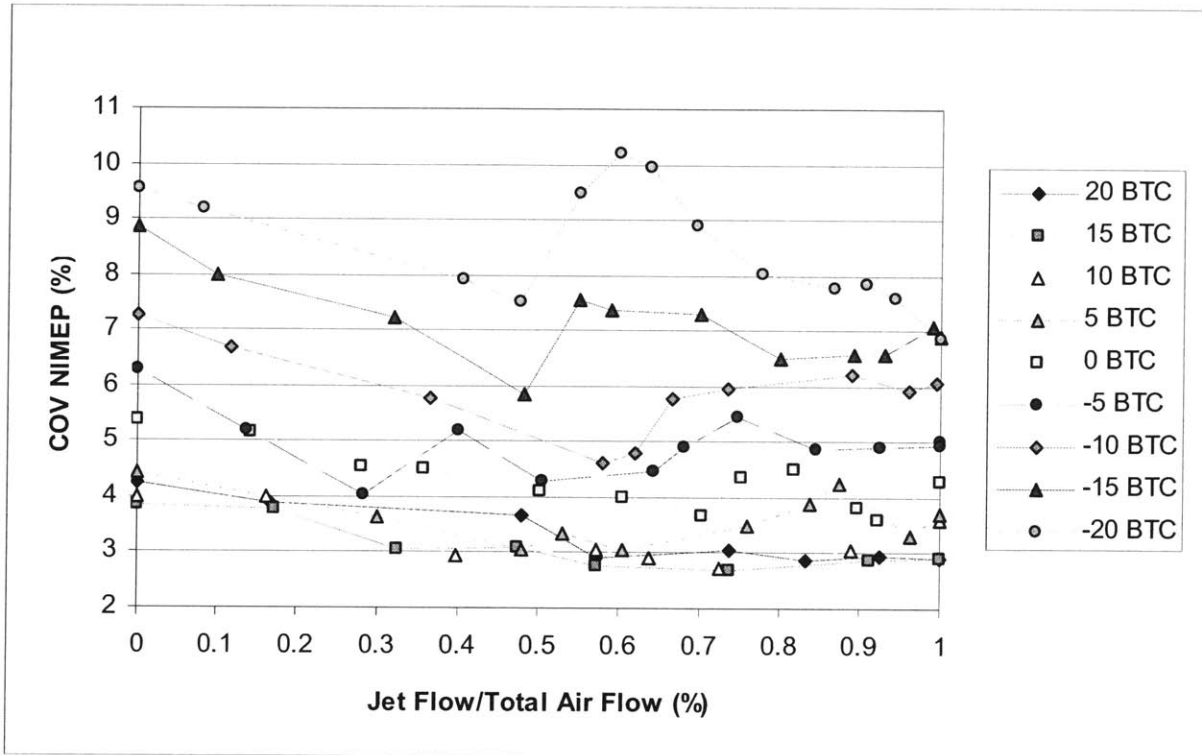
Figure 4-5   Swirl Jet: COV NIMEP vs. Percent Jet Flow. The data are taken across nine spark timings with the swirl jet used to increase turbulence.
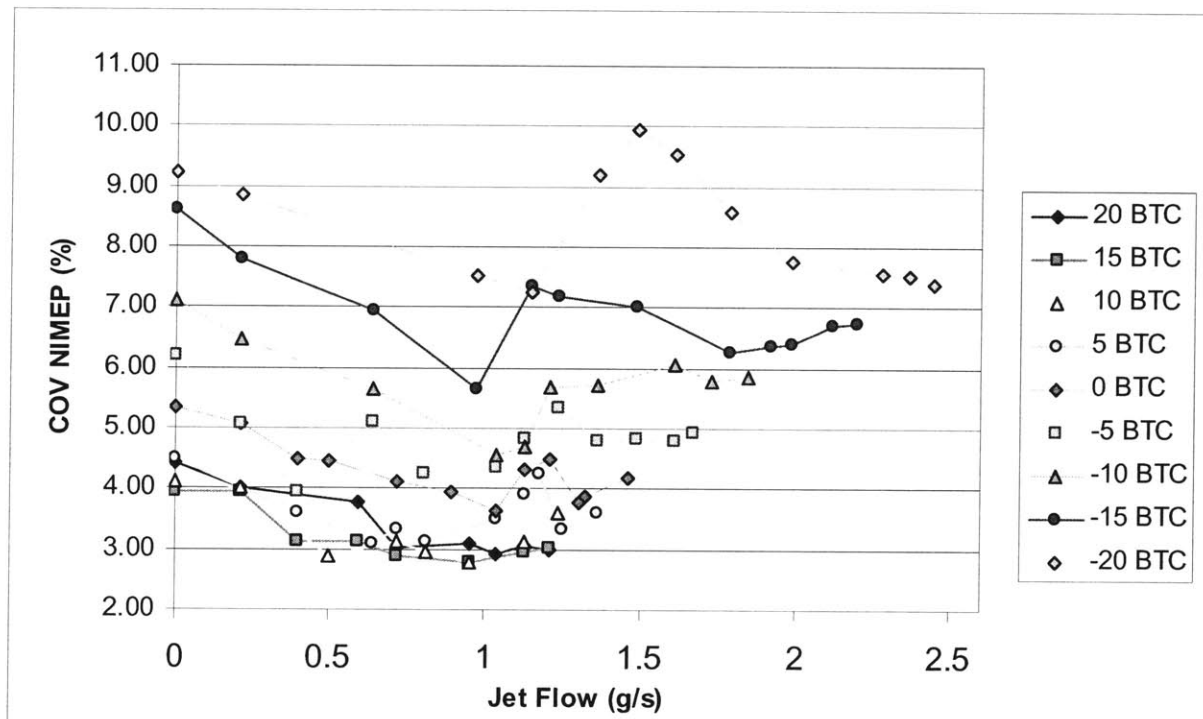
Figure 4-6   Swirl Jet: COV NIMEP vs. Jet Mass Flow. A minimum occurs at many of the spark timings around 1.1 g/s.
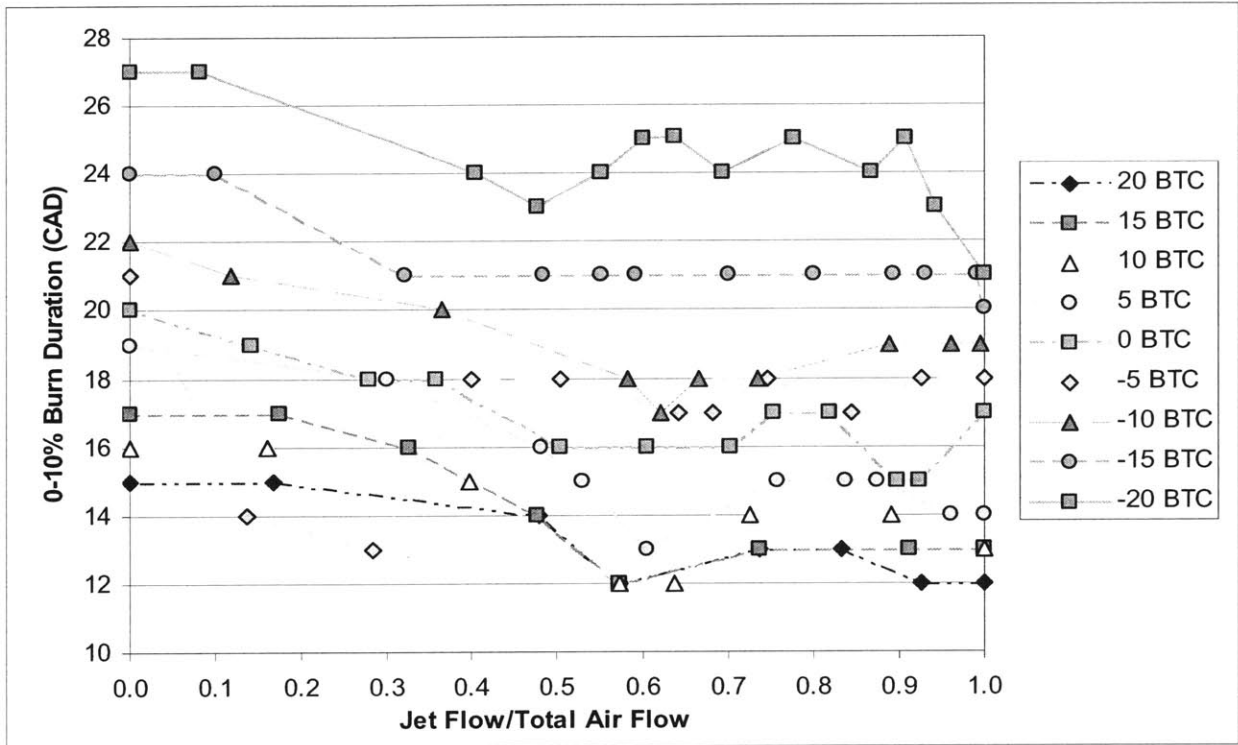
Figure 4-7   Swirl Jet: 0-10% Burn Duration vs. Percentage Jet Flow.
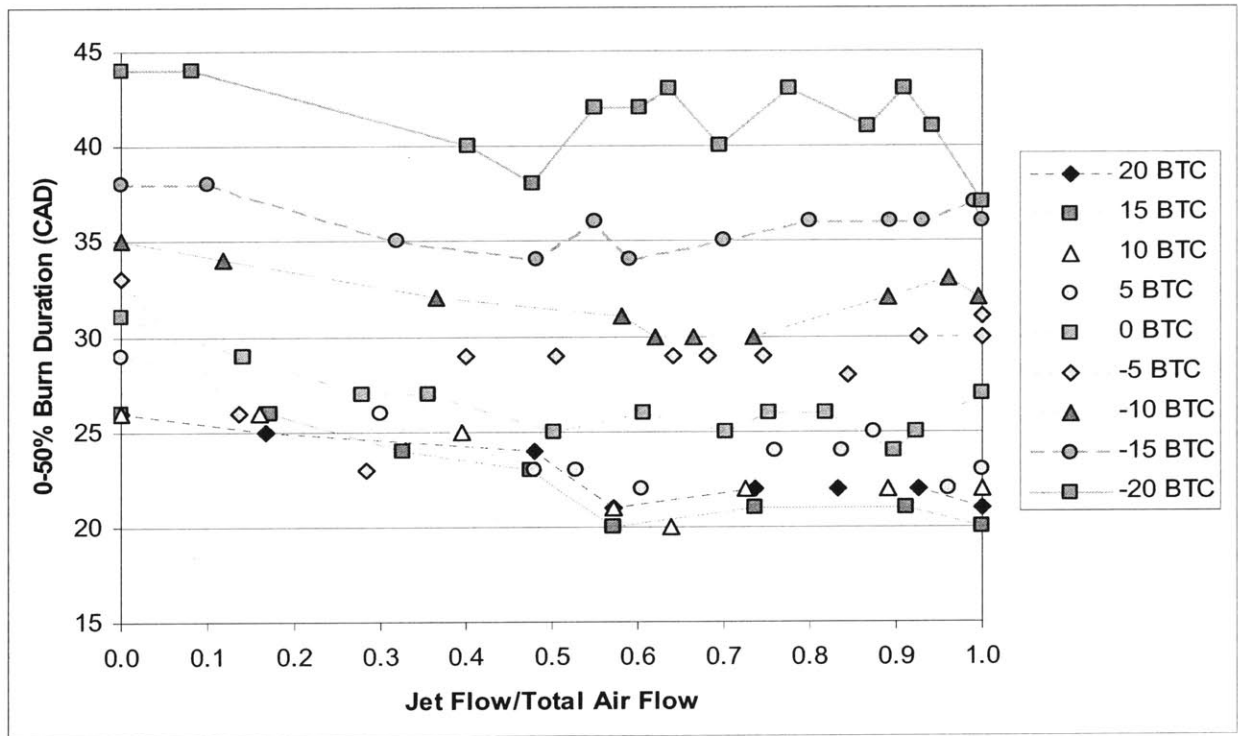
Figure 4-8   Swirl Jet: 0-50% Burn Duration vs. Percentage Jet Flow.
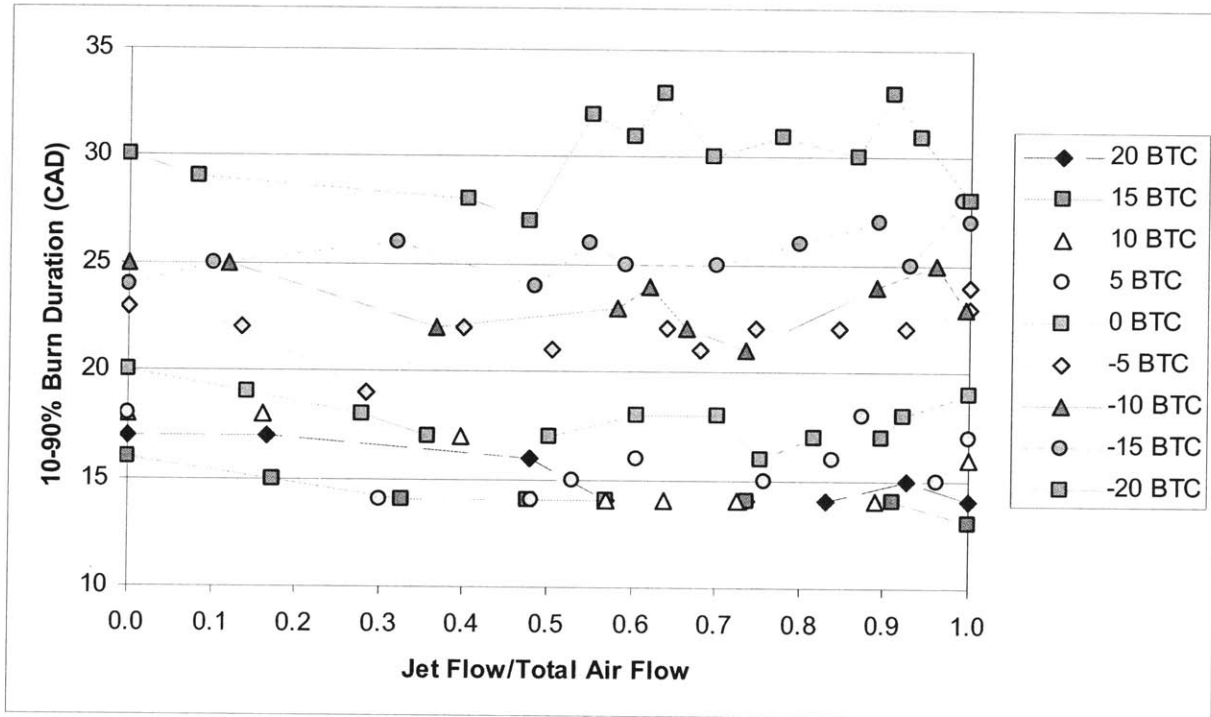
Figure 4-9   Swirl Jet: 10-90% Burn Duration vs. Percentage Jet Flow.
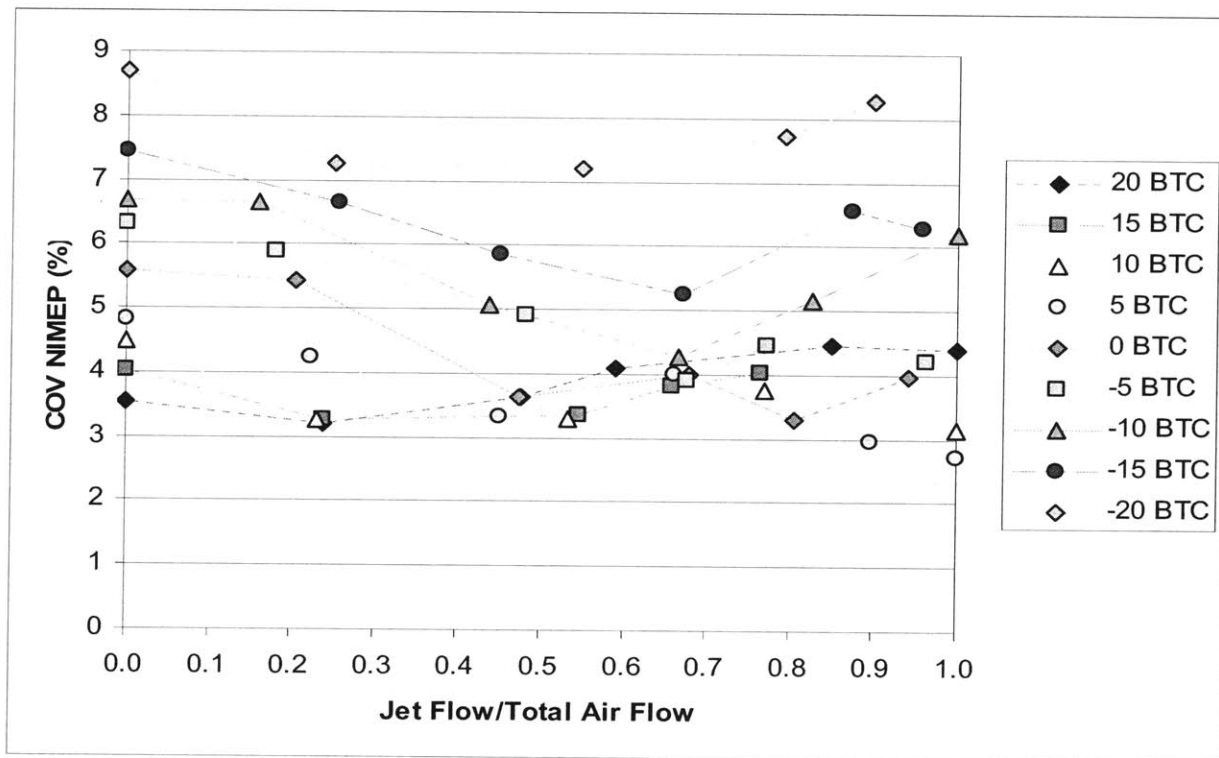
Figure 4-10   Tumble Jet: COV NIMEP vs. Percentage Jet Flow.
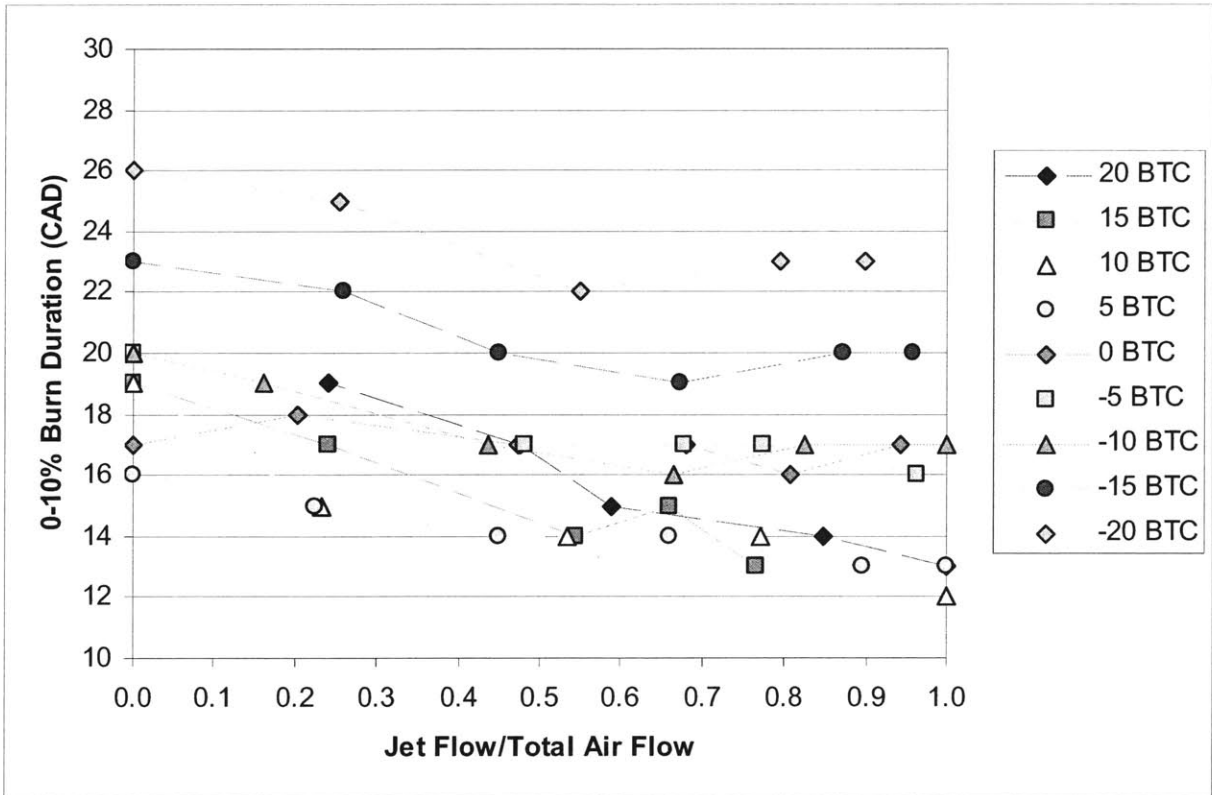
Figure 4-11   **Tumble Jet: 0-10% Burn Duration vs. Percentage Jet Flow.**
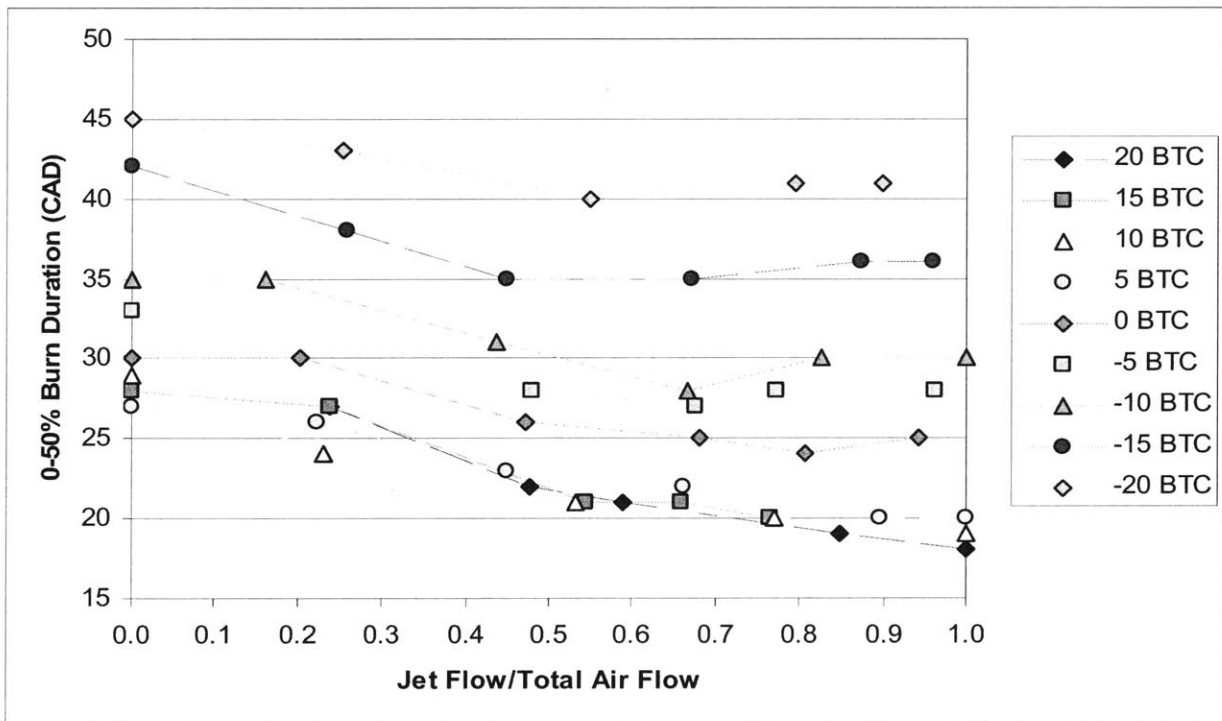
Figure 4-12   **Tumble Jet: 0-50% Burn Duration vs. Percentage Jet Flow.**
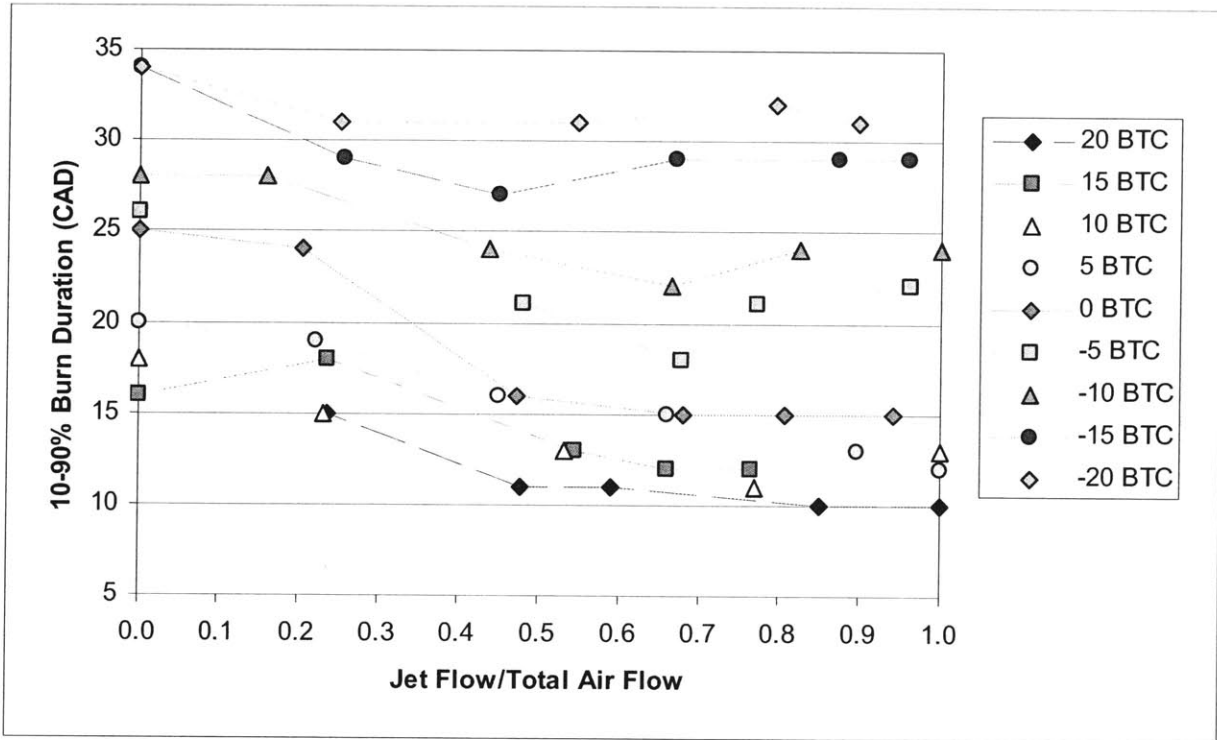
Figure 4-13   Tumble Jet: 10-90% Burn Duration vs. Percentage Jet Flow.
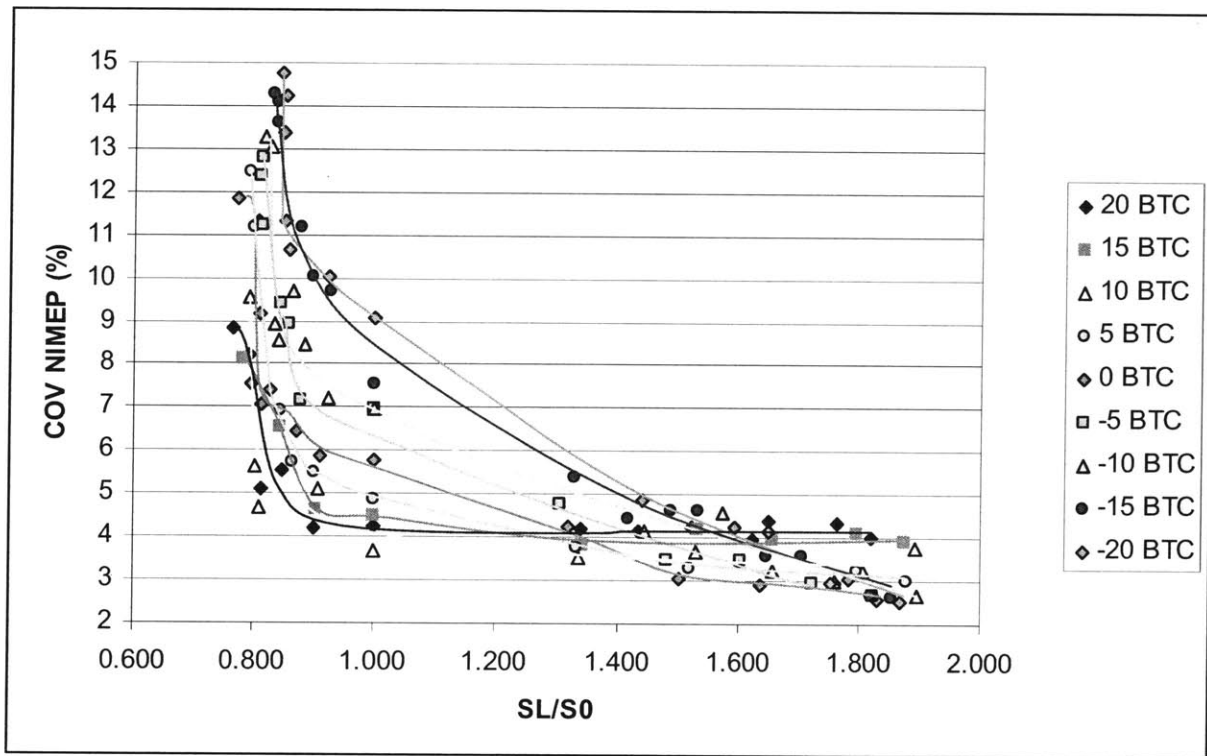
Figure 4-14   Laminar Flame Speed Change Tests: COV NIMEP vs. Relative Laminar Flame Speed.
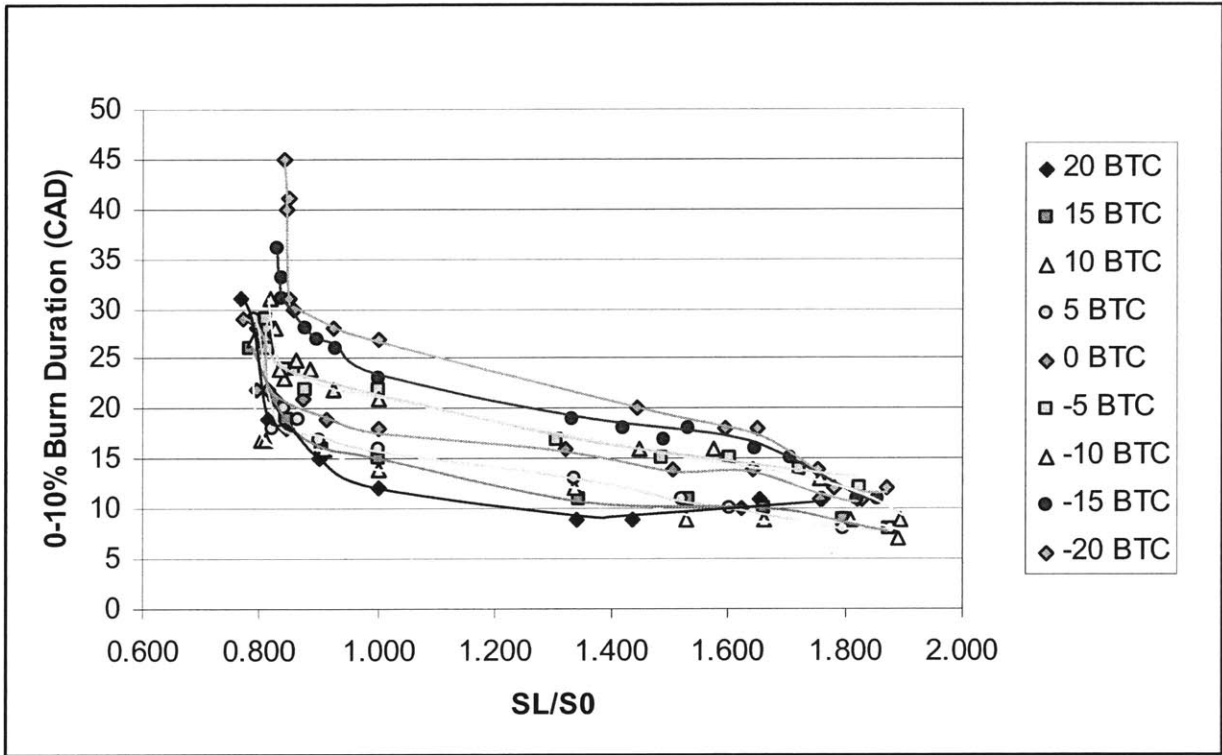
Figure 4-15   Laminar Flame Speed Change Tests: 0-10% Burn Duration vs. Relative Laminar Flame Speed.
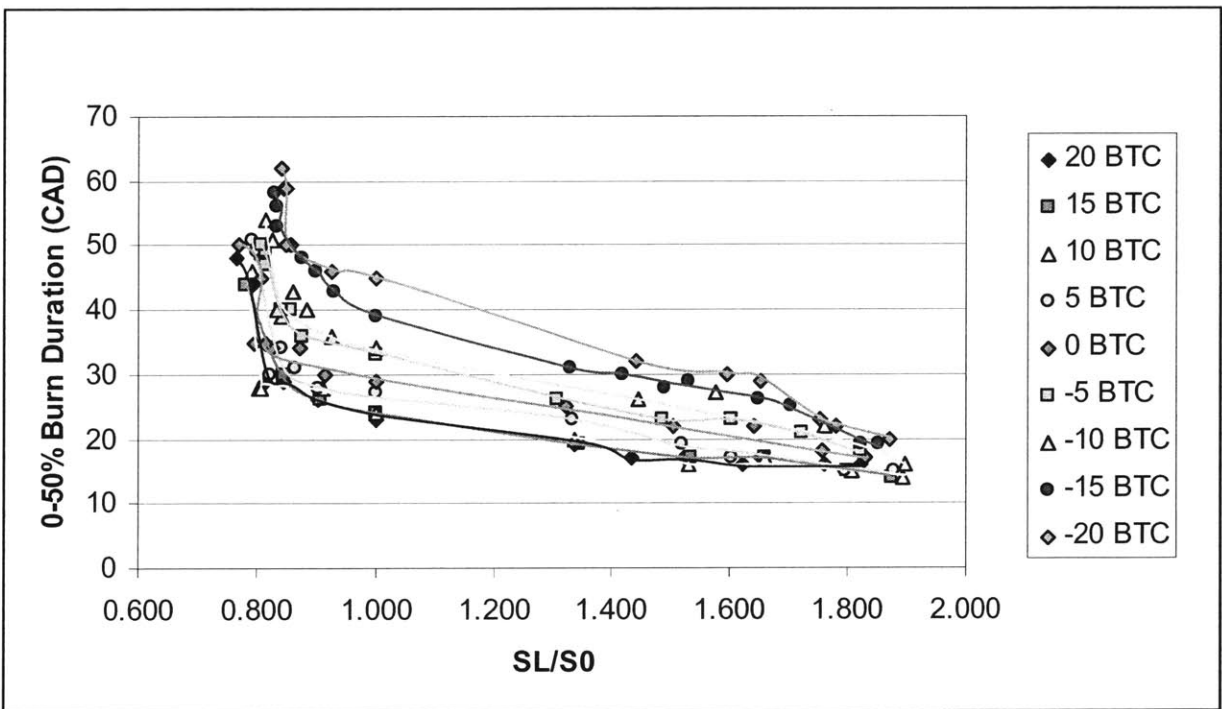
Figure 4-16   Laminar Flame Speed Change Tests: 0-50% Burn Duration vs. Relative Laminar Flame Speed.
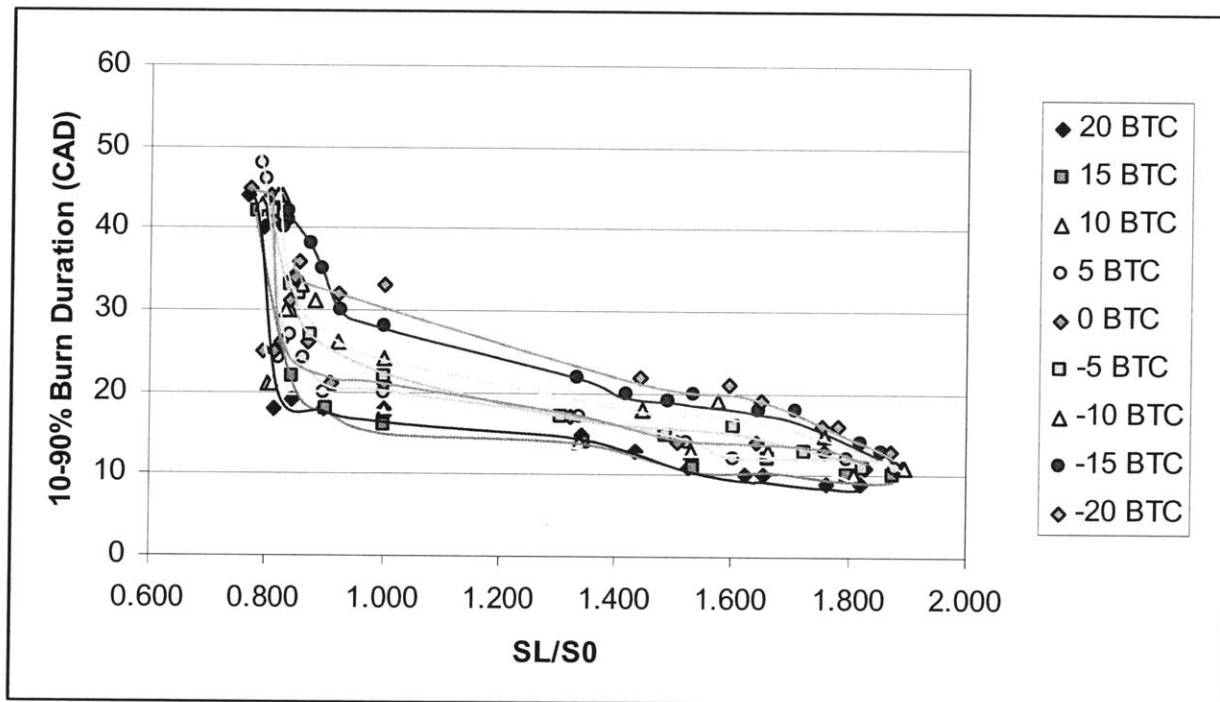
Figure 4-17   **Laminar Flame Speed Change Tests: 10-90% Burn Duration vs. Relative Laminar Flame Speed.**
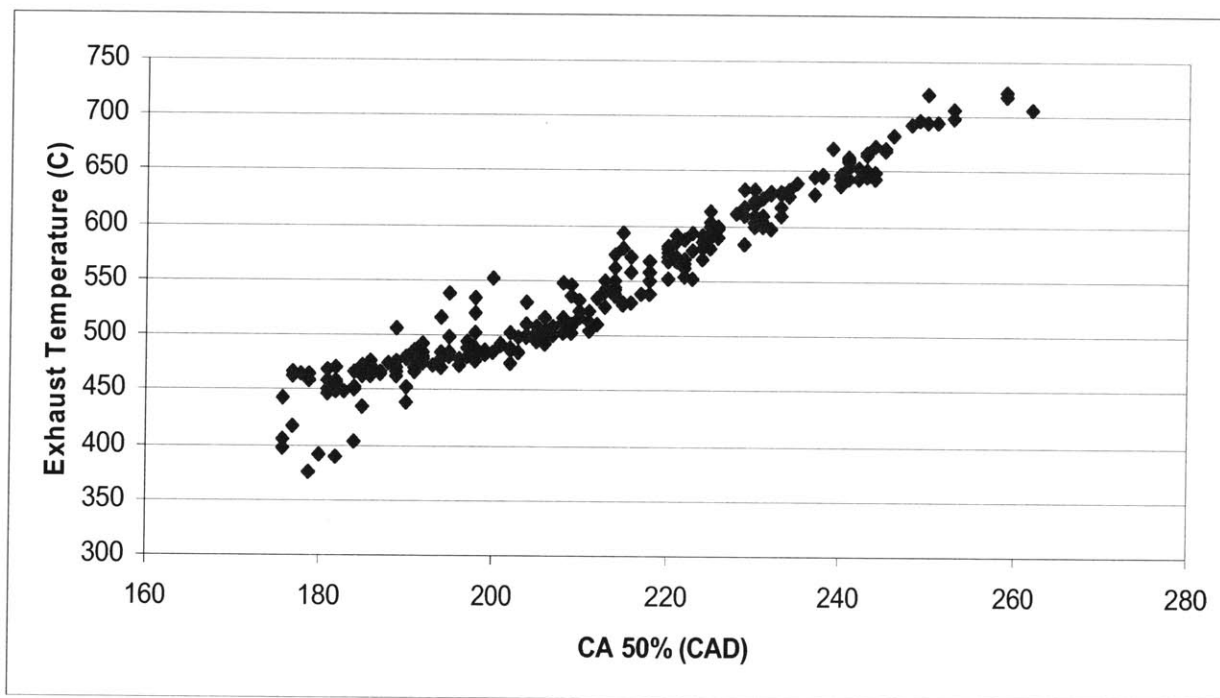
Figure 4-18   **Global Data Set: Exhaust Temperature vs. CA 50%.**
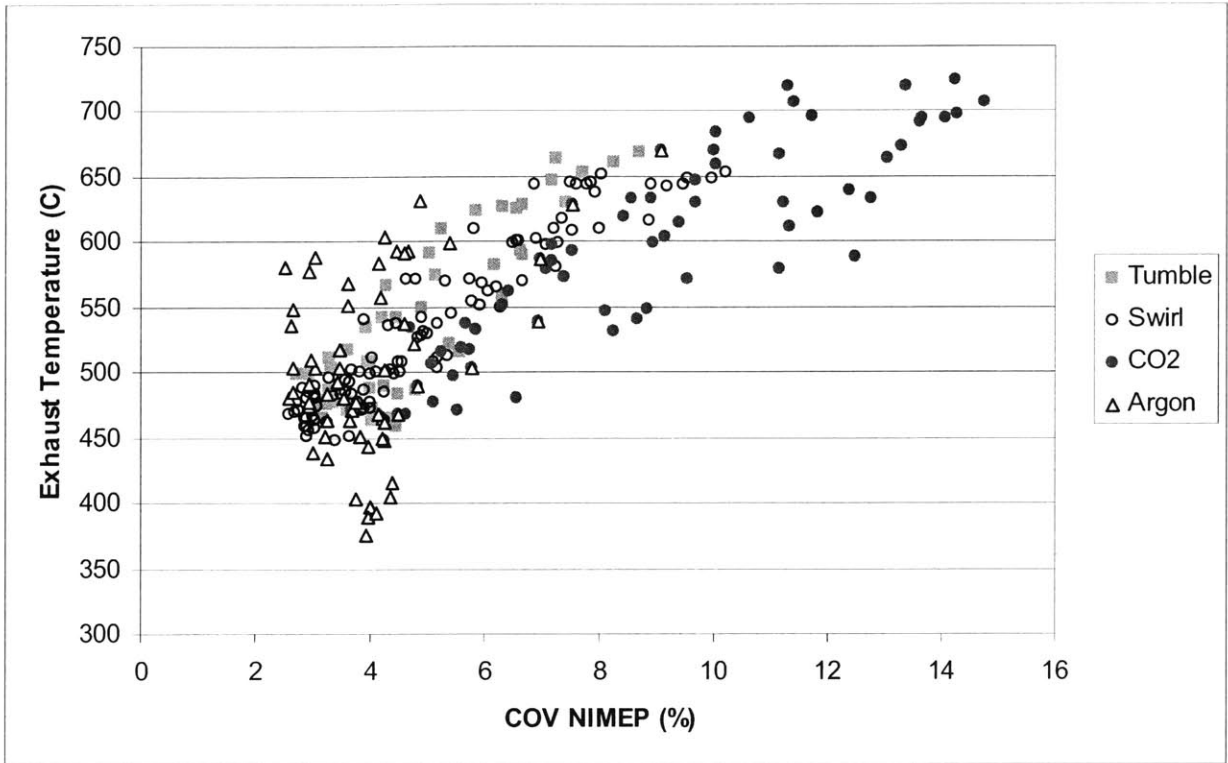
Figure 4-19   **Global Data Set: Exhaust Temperature vs. COV of NIMEP.**
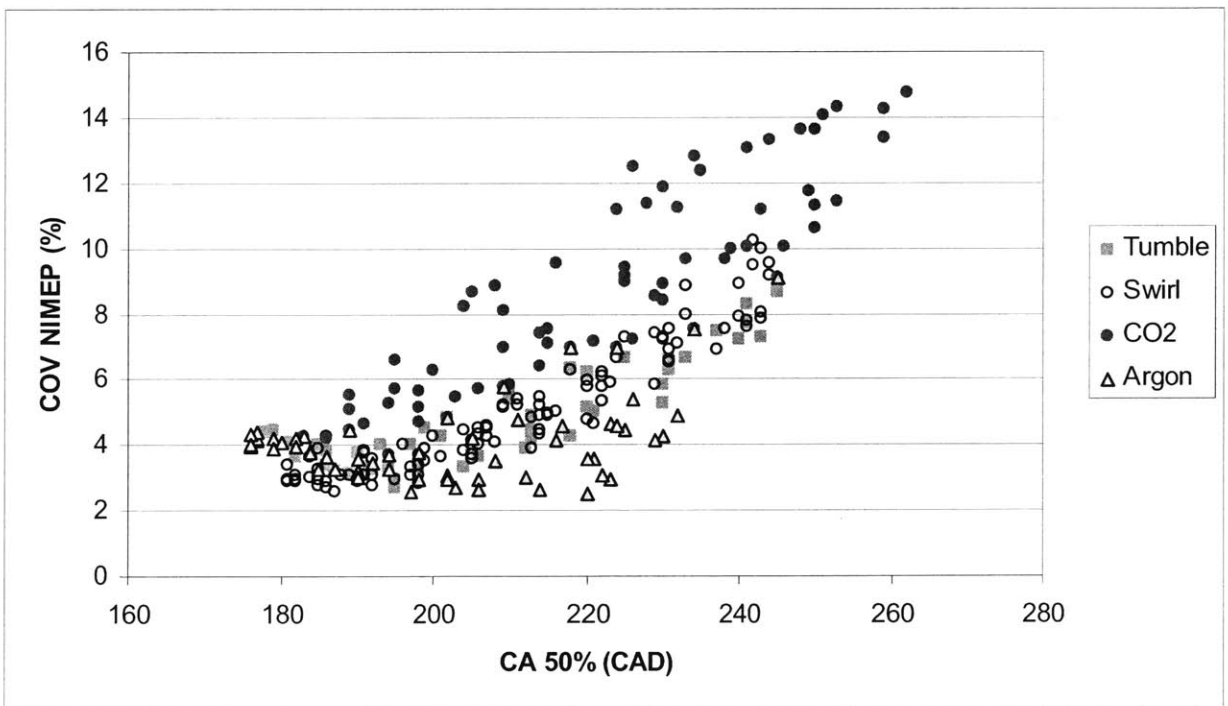
Figure 4-20   **Global Data Set: COV NIMEP vs. CA 50%.**
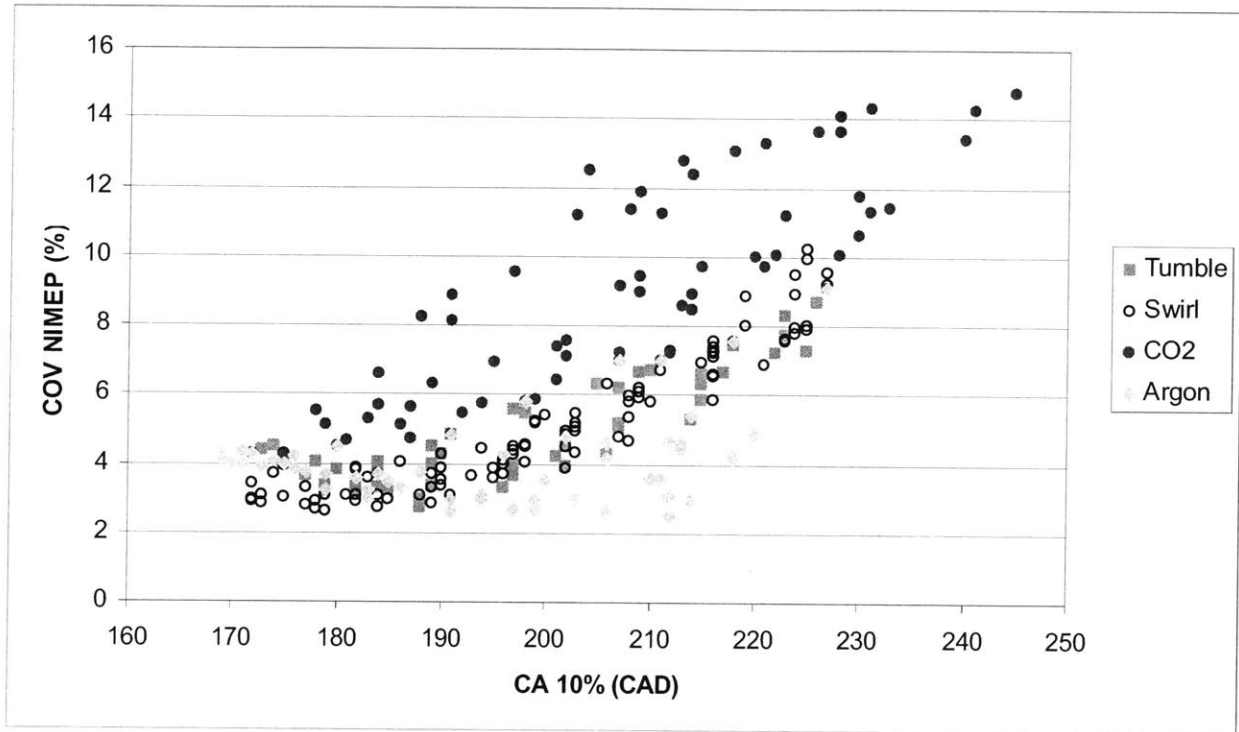
Figure 4-21   **Global Data Set: COV NIMEP vs. CA 10%.**
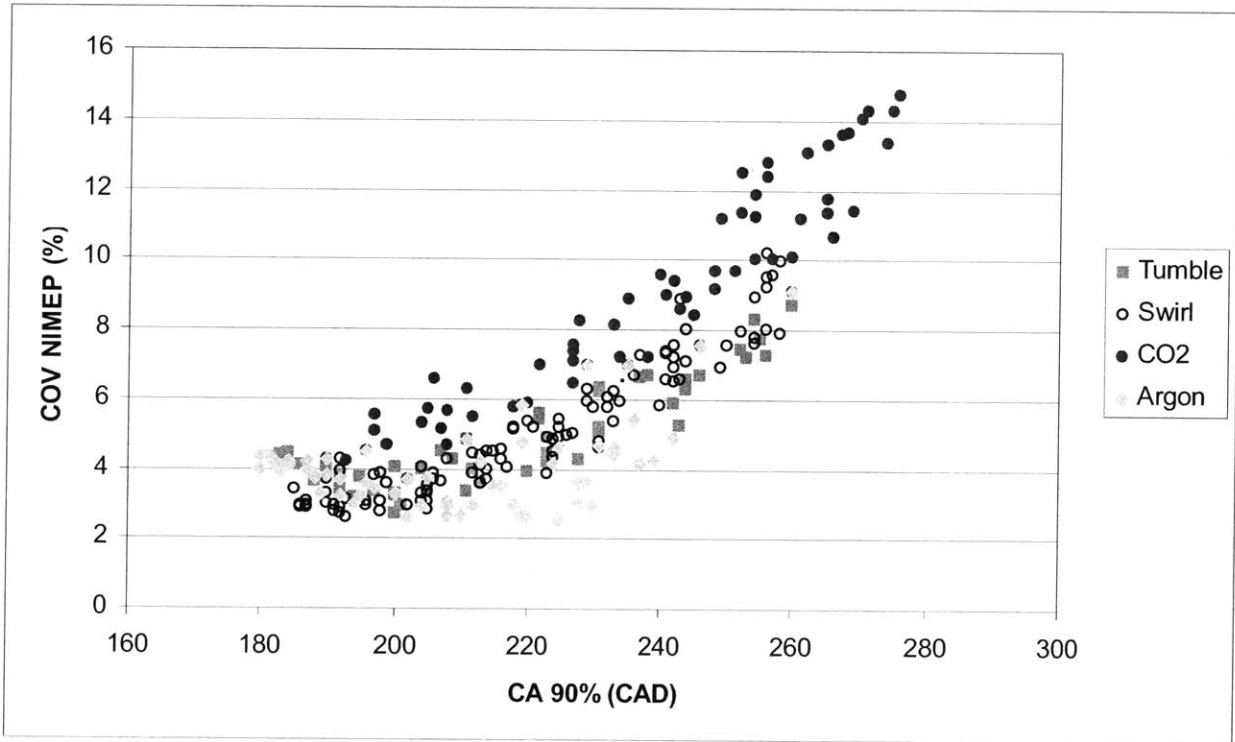
Figure 4-22   **Global Data Set: COV NIMEP vs. CA 90%.**
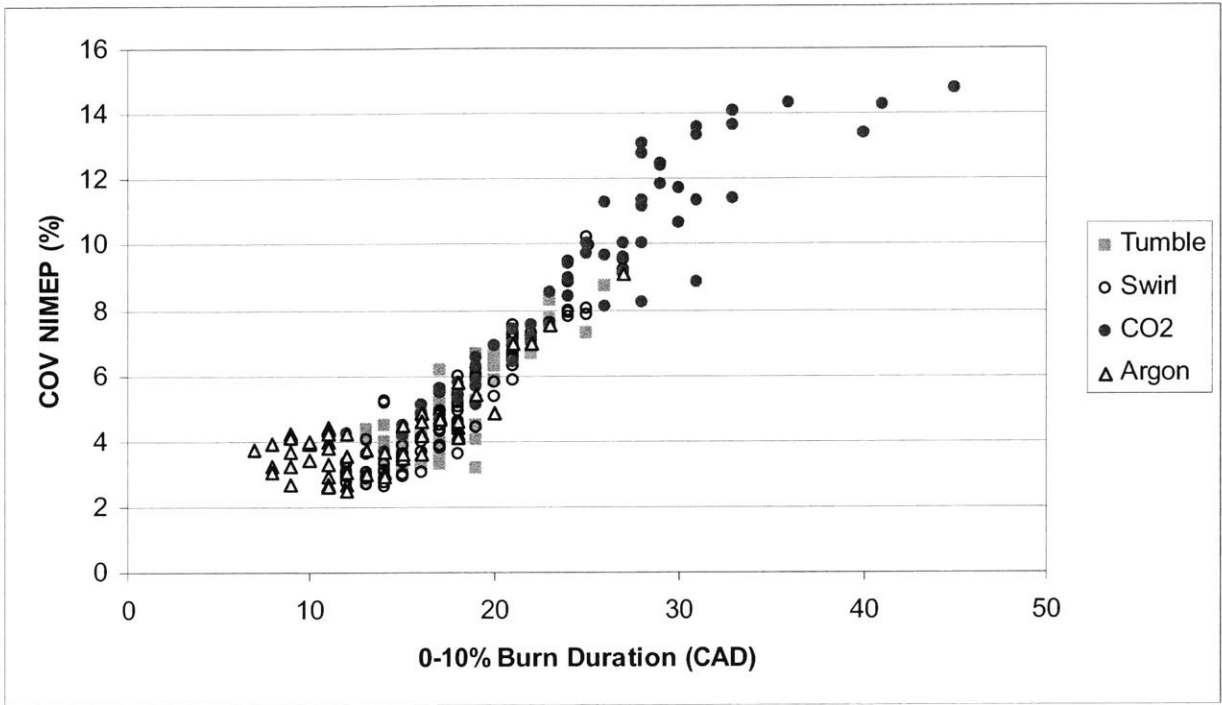
Figure 4-23   Global Data Set: COV NIMEP vs. O-10% Burn Duration.
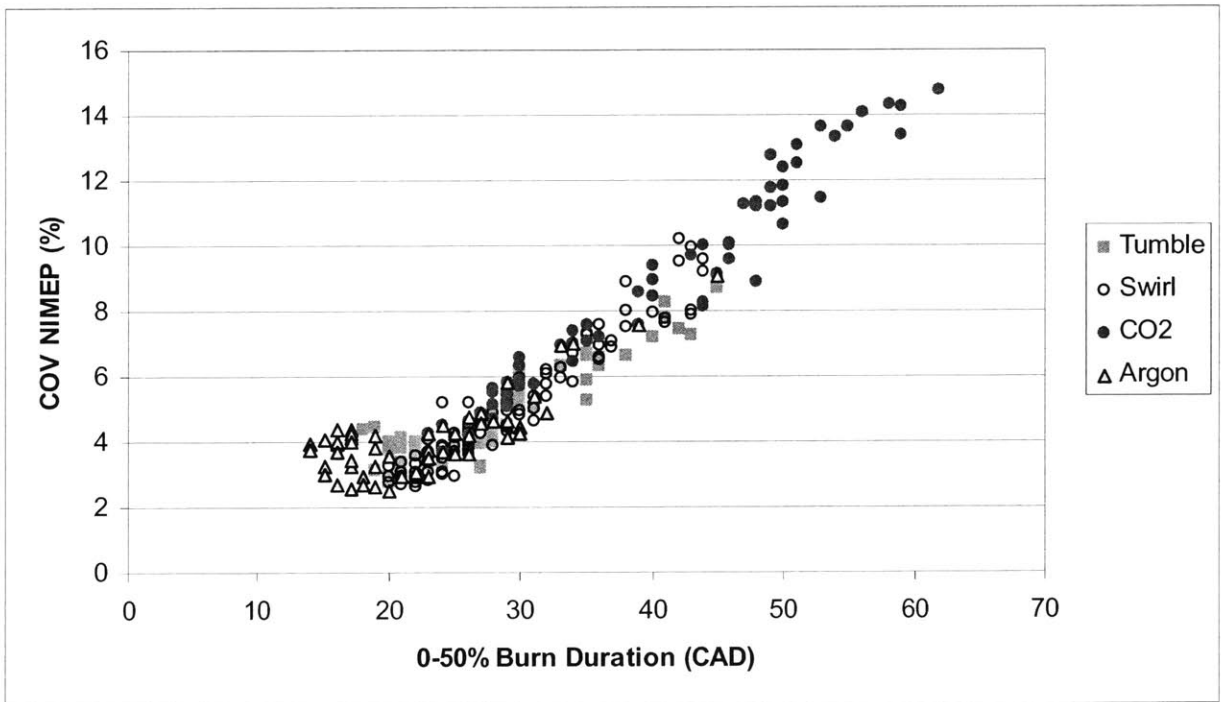
Figure 4-24   Global Data Set: COV NIMEP vs. 0-50% Burn Duration.
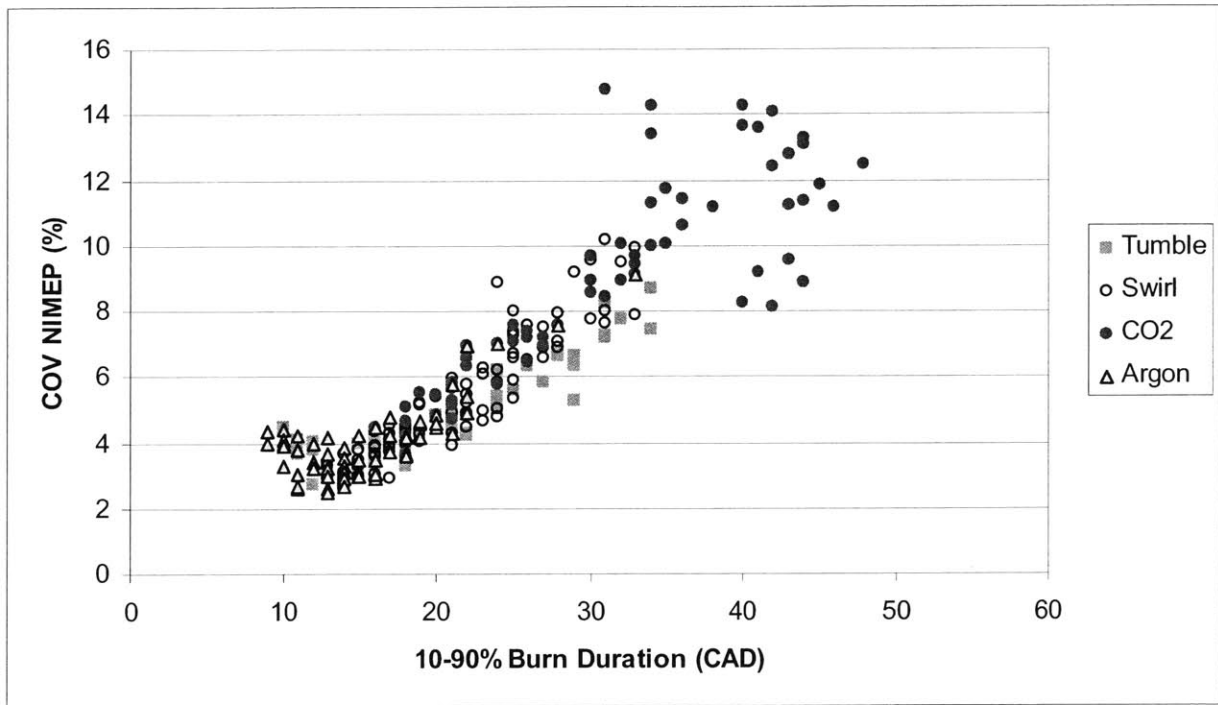
Figure 4-25   Global Data Set: COV NIMEP vs. 10-90% Burn Duration.

Chapter 5 Conclusion

An experimental study on combustion stability was conducted to further understand the causes of cycle-by-cycle variability in a spark-ignition engine. Combustion experiments were conducted in which in-cylinder turbulence was varied via an added air jet. Also, combustion experiments were conducted where the inert gas in the mixture was varied to change the laminar flame speed of the mixture. These tests were done at conditions to simulate fast-idle: 1400rpm, 2.6bar NIMEP, equivalence ratio equal to 1.00, and 20°C coolant temperature. COV of NIMEP, burn duration, combustion phasing, and exhaust temperature data from these tests were examined.

The two jet orientations improved COV to varying degrees. The swirl jet improved COV by about 30% at each spark timing, ranging from 28% and 35% improvements. The tumble jet showed a wider range of effectively, improving middle-range timings by over 40% and by improving early and very late spark timings by less than 20%, as little as 10% at 20° BTC. Burn durations generally followed the trends of COV.

The laminar flame speed tests yielded reduced burn duration and COV in a linear fashion as the laminar flame speed was increased. As it was decreased, COV and burn duration increased linearly until at a point common to all spark timings, COV and burn duration increased significantly, non-linearly. Laminar flame speed enhancement had an increasing impact on COV and burn duration as timing was retarded, even to the point that later timing curves featured lower COV points than earlier timing curves.

Plots featuring the global data set illustrated qualitative relationships between exhaust temperature, COV, burn duration, and combustion phasing. Exhaust temperature showed tight linear correlation to CA 50%; however, it showed a much weaker linear correlation with COV. This is consistent with the fact that COV showed a weak correlation with CA 50%. In this plot, it was clear that the turbulence data held a much tighter correlation than the laminar data did. Compared to plots of COV vs. CA 10% and CA 90%, it became clear that the correlation between COV and the combustion phase became tighter as the combustion phase became later. Finally, COV was plotted against 0-10%, 0-50%, and 10-90% burn duration, and it correlated well, linearly with each of them, except for the very shortest burn duration points where COV leveled off instead of continuing to decrease.

From comparison between laminar and turbulent COV data, it is likely that additional turbulence causes competing effects that do not all reduce CCV. Retarding the spark timing reduces turbulent intensity, which increases CCV by allowing more random walk of the flame kernel; however, it also seems to alleviate another effect. This is shown because increasing the laminar flame speed improved COV beyond the point that it improved the COV of earlier spark timings, which presumably featured more turbulence.

Further study is necessary to obtain quantitative relationships between these factors. In-cylinder turbulence data would be necessary for this.

References

[1]   Hinze, P.C. and Cheng, W.K. "Assessing the Factors Affecting SI Engine Cycle-to-Cycle Variations at Idle," Twenty-Seventh Symposium on Combustion, The Combustion Institute, pp. 2119-2126, 1998.

[2]   Ozdor, N., Dulger, M., and Sher, E. "An Experimental Study of the Cyclic Variability in Spark Ignition Engines," SAE paper 960611, 1996.

[3]   Ozdor, N., Dulger, M., and Sher, E. "Cyclic Variability in Spark Ignition Engines: A Literature Survey," SAE paper 940987, 1994.

[4]   Eastwood, Peter, *Critical Topics in Exhaust Gas Aftertreatment.* Research Studies Press Ltd., Baldock, Hertfordshire, England, 2000.

[5]   Heywood, John B., *Internal Combustion Engine Fundamentals.* McGraw-Hill, Inc., New York, NY, 1988.

[6]   Russ, S., Thiel, M., and Lavoie, G. "SI Engine Operation with Retarded Ignition: Part 2-HC Emissions and Oxidation," SAE paper 1999-01-3507, 1999.

[7]   Hallgren, B. and Heywood, J. "Effects of Substantial Spark Retard on SI Engine Combustion and Hydrocarbon Emissions," SAE paper 2003-01-3237, 2003.

[8]   Hill, P.G., "Cyclic Variations and Turbulence Structure in Spark-Ignition Engines," *Combustion and Flame*, Vol. 72. pp. 73-89, 1988.

[9]   Keck, J.C., Heywood, J.B., and Noske, G. "Early Flame Development and Burning Rates in Spark Ignition Engines and Their Cyclic Variability," SAE paper 870164, 1987.

[10]   Beretta, G.P., Rashidi, M., and Keck, J.C. "Turbulent Flame Propagation and Combustion in Spark Ignition Engines," *Combustion and Flame.* Vol. 52. pp. 217-245, 1983.

[11]   Bianco, Y., Cheng, W.K., and Heywood, J.B. "The Effects of Initial Flame Kernel Conditions on Flame Development in SI Engine," SAE paper 912402, 1991.

[12]   Russ, S., Peet, G., and Stockhausen, W. "Measurements of the Effect of In-Cylinder Motion on Flame Development and Cycle-to-Cycle Variations Using an Ionization Probe Head Gasket," SAE paper 970507, 1997.

[13]   Pischinger, S. and Heywood, J.B., "A Model for Flame Kernel Development in a Spark Ignition Engine," Twenty-Third Symposium (International) on Combustion, The Combustion Institute, pp. 1033-1040, 1990.

[14]   Pischinger, S. and Heywood, J.B. "How Heat Losses to the Spark Plug Affect Flame Kernel Development in an SI-Engine," SAE paper 900021, 1990.

[15]   Smith, J.R. "The Influence of Turbulence on Flame Structure in an Engine," in T. Uzkan (ed.), *Flows in Internal Combustion Engines,* pp. 67072, ASME, New York, 1982.

[16]   Hacohen, J., Belmont, M. R., Yossefi, D., Thomas, J. C., and Thurley, R. "The Effect of Flame Kernel Surface Stretch on Cyclic Variability in an SI Engine," SAE paper 932717, 1993.

[17]   Lee, K.H. and Foster, D.E. "Cycle-by-cycle Variations in Combustion and Mixture Concentration in the Vicinity of Spark Plug Gap," SAE paper 950814, 1995.

[18]   Sher, E. and Keck, J.C., "Spark Ignition of Combustible Gas Mixture," Combustion and Flame, Vol. 66, pp. 17-25, 1986.

[19]   Witze, P.O. "The Effect of Spark Location on Combustion in a Variable-Swirl Engine," SAE paper 820044, 1982.

[20]   Rassweiler, G. M. and Withrow, L. "Motion Pictures of Engine Flames Correlated with Pressure Cards," *SAE Transactions.,* Vol. 83, pp. 185-204, 1938.

[21]   Rhodes, D.B. and Keck, J.C. "Laminar Burning Speed Measurements of Indolene-Air-Diluent Mixtures at High Pressures and Temperature," SAE paper 850047, 1985.

Appendix A: Useful Parameters

Fluid Mechanics Definitions

The instantaneous velocity of a steady turbulent flow U features two components, a mean velocity $\overline{U}$ and a fluctuating velocity u as in Equation A-1.

$$U(t) = \overline{U} + u(t) \tag{A-1}$$

The mean velocity component $\overline{U}$ is the time average of $U(t)$.

$$\overline{U} = \lim_{\tau \to \infty} \frac{1}{\tau} \int_{t_0}^{t_0 + \tau} U(t) dt \tag{A-2}$$

In an engine, the velocity is unsteady. It can be written as a function of the crank angle of the engine θ for a particular cycle i.

$$U(\theta, i) = \overline{U}(\theta, i) + u(\theta, i) \tag{A-3}$$

Here, $\overline{U}(\theta, i)$ is the time-average velocity of the duration of some crank angles in a particular cycle. The averaging period is long compared to the small-scale velocity fluctuation but is short to resolve the in-cylinder bulk motion. An ensemble average of the velocity over many cycles is defined for a specific crank angle as in Equation A-4.

$$\overline{U}_{EA}(\theta) = \frac{1}{N_c} \sum_{i=1}^{N_c} U(\theta, i) \tag{A-4}$$

N_c is the number of considered cycles. $\hat{U}(\theta, i)$ is defined as the difference between the time-average velocity of a crank angle of a particular cycle and the cycle-by-cycle average for the crank angle. This is the cycle-by-cycle mean velocity variation.

$$\hat{U}(\theta, i) = \overline{U}(\theta, i) - \overline{U}_{EA}(\theta) \tag{A-5}$$

Incorporating this and the ensemble average, Equation A-6 shows the velocity in terms of the average velocity for many cycles $\overline{U}_{EA}(\theta)$, the average deviation from it for a particular cycle $\hat{U}(\theta, i)$, and the random fluctuation in a given cycle u.

$$U(\theta, i) = \overline{U}_{EA}(\theta) + \hat{U}(\theta, i) + u(\theta, i) \tag{A-6}$$

The turbulent intensity u' defines the fluctuating velocity component u by its root mean square value [5].

$$u' = \lim_{\tau \to \infty} \left(\frac{1}{\tau} \int_0^{t_0 + \tau} u^2 dt \right)^{1/2} \tag{A-7}$$

Net Indicated Mean Effective Pressure and Covariance

Net Indicated Mean Effective Pressure (NIMEP) is used throughout this project as an indicator of torque. It is defined and related to torque as follows. Covariance (COV) is used to measure the cycle-to-cycle variations of NIMEP.

$$NIMEP = \frac{W_{c,i}}{V_d} \tag{A-8}$$

$W_{c,i}$ is the indicated work per cycle, and V_d is the displace volume of the cylinder. Work per cycle is defined by the integral of cylinder pressure with respect to change in volume.

$$NIMEP = \frac{W_{c,i}}{V_d} = \frac{1}{V_d} \oint p \cdot dV \tag{A-9}$$

The torque output of the engine T is related to NIMEP by displaced volume V_d and the number of revolutions per cycle n_r.

$$T = \frac{V_d}{2\pi \cdot n_r} NIMEP - T_{friction} - T_{accessory} \tag{A-10}$$

$T_{friction}$ and $T_{accessory}$ are the torques acting against the engine due to friction and accessory loads. If these are held constant by keeping engine speed constant and by engine control, torque and NIMEP are proportional. Cycle-by-cycle torque variations are proportional to cycle-to-cycle variations in NIMEP, which is estimated by covariance, as in Equation A-11 [5].

$$COV_{NIMEP} = \frac{\sigma_{NIMEP}}{Avg_{NIMEP}} \cdot 100\% \tag{A-11}$$

COV_{NIMEP} indicates the variation in the pressure trace when NIMEP is taken over many cycles. σ_{NIMEP} is the standard deviation and Avg_{NIMEP} is the average NIMEP.

Burn Duration and Combustion Phasing

The percent burn durations were calculated using the Rassweiler and Withrow method [20]. This simple method requires only the pressure at a given crank angle degree $p(\theta)$, the pressure at ignition p_0, the pressure at the end of combustion, p_f and the exponent n from the polytropic relation in Equation A-12.

$$pV^n = k \tag{A-12}$$

k is a constant. This equation is used to relate the pressure and volume of the initial unburned gas to those of the unburned gas during combustion and the pressure and volume of the final burned gas to those of the burned gas during combustion as follows.

$$p_0 V_{u,0}^n = pV_u^n \qquad\qquad p_f V_{f,b}^n = pV_b^n \tag{A-13}$$

$$V_{u,0} = V_u \left(\frac{p}{p_0} \right)^{1/n} \qquad\qquad V_{b,f} = V_b \left(\frac{p}{p_f} \right)^{1/n} \tag{A-14}$$

Next, burned mass fraction is related to volume fraction. The in-cylinder pressure rise is due to a combustion component Δp_c and a compression component Δp_v.

$$\Delta p = \Delta p_c + \Delta p_v \tag{A-15}$$

The pressure and volume change due to the compression component are estimated using an isentropic relation.

$$p_i V_i^n = p_j V_j^n \tag{A-16}$$

Incorporating this into Equation A-15 yields Equation A-17.

$$\Delta p_v = p_i \left[\left(\frac{V_i}{V_j} \right)^n - 1 \right] \tag{A-17}$$

The assumption is made that for a given mass of mixture burned, a corresponding pressure rise results. The pressure rise is actually due to fuel chemical energy release, but this assumption provides a reasonable estimate.

$$\frac{m_{b(i)}}{m_{b(total)}} = \frac{\sum_0^i \Delta p_c}{\sum_0^N \Delta p_c} \tag{A-18}$$

Here, N is the total number of crank angles considered. Using Equations A-15 to A-18, burned mass fraction is related to volume change.

$$x_b = 1 - \frac{V_{u,0}}{V_0} = \frac{V_{b,f}}{V_f} \tag{A-19}$$

Relating Equations A-14 and A-19, an equation relating burned mass fraction to in-cylinder pressure, n, volume, pressure at ignition, and pressure at the end of combustion results [5,20].

$$x_b = \frac{p^{1/n}V - p_0^{1/n}V_0}{p_f^{1/n}V_f - p_0^{1/n}V_0}$$

<div align="right">(A-20)</div>

To calculate these parameters, many cycles of data, specifically 320, are taken and an average cycle pressure trace is found. An example is shown in Figure A-1.
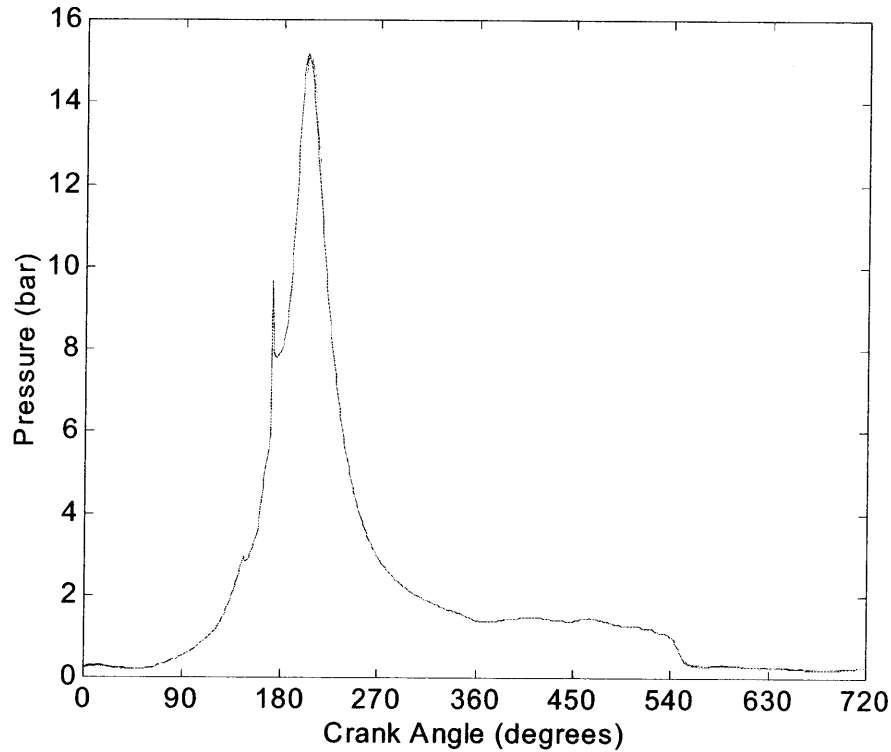
Figure A-1   A Typical Pressure Trace. Spark noise causes the spike before the pressure rise.

Then, $\log(p)$ vs. $\log(V)$ are plotted. A line is fitted to the last 60 points before EVO, and the slope of this line is used as an estimate for n. The spark timing is used as the combustion starting point. The combustion ending point is estimated as the point where the log(p) vs. log(V) plot becomes tangent with part of the trace during the expansion stroke that is a straight line, as shown in Figure A-2.
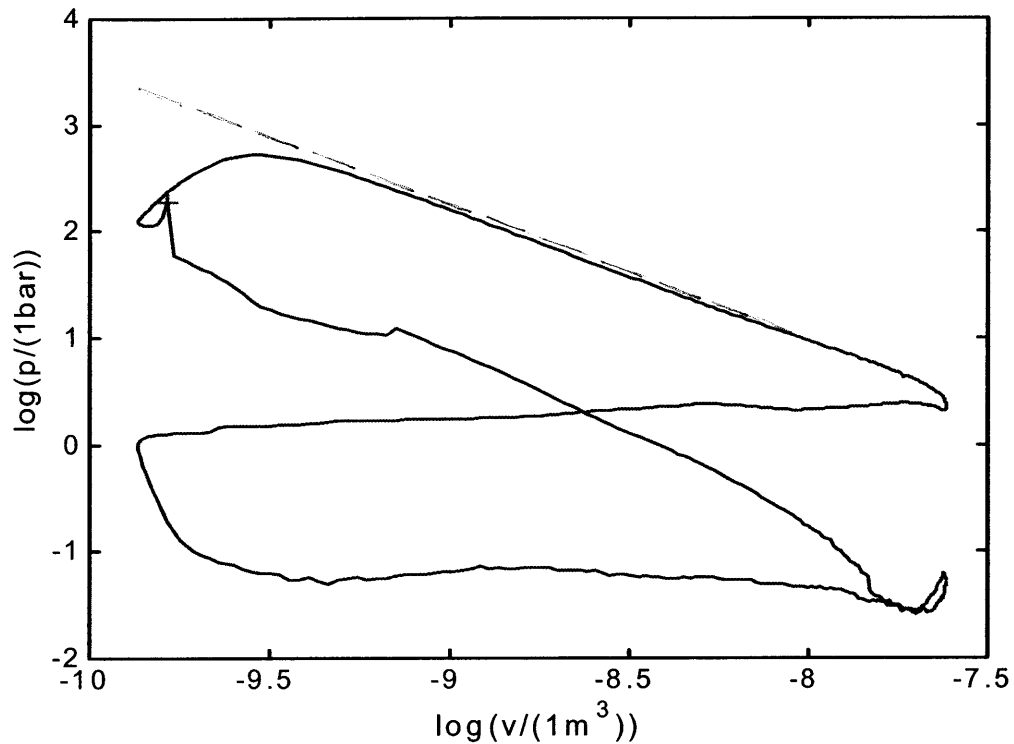
Figure A-2   log(*p*) vs. log(*V*) of a Typical Pressure Trace. The straight line of the trace during the expansion stroke is used to find *n*. The point where the trace becomes tangent to it is estimated to be the end of combustion. The red cross marks the spark point.

Using the acquired burned mass fraction curve, the crank angle degrees of 10%, 50%, and 90% burn are found. An example of such a curve is shown in Figure A-3 Burn durations are computed by finding the difference between each of these points and between them and the spark crank angle. The aforementioned spark noise is the cause of jagged part of the compression stroke near the beginning of combustion. The noise prevented accurate assessment of the 0-2% burn duration.
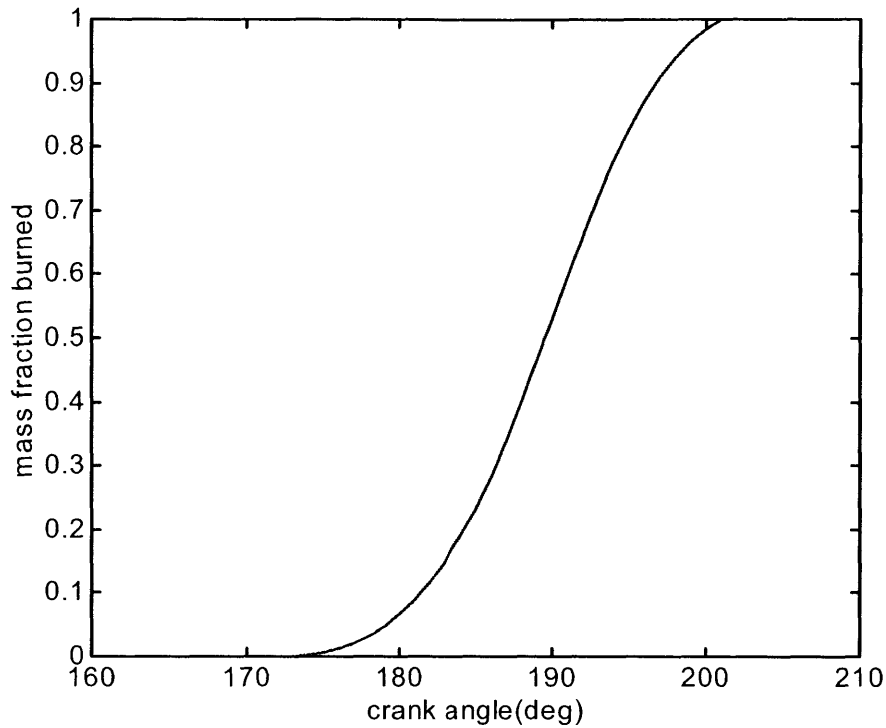
Figure A-3   **A Burned Mass Fraction vs. Crank Angle Example Plot. This example plot illustrates the rate of the burn during combustion.**

Relative Laminar Flame Speed

Adding diluent, non-reactive species, to an unburned mixture can influence the laminar flame speed. The diluent changes the thermodynamic properties of the mixture. For example, substituting CO_2 for the N_2 in air would reduce the temperature of the burned gas and the flame speed. Substituting Ar would do the opposite.

An empirical way to account for the above dilution effect is to correlate the flame speed to the adiabatic flame temperature, the value of which is a measure of the overall effect of thermodynamic properties on flame behavior. The data of [21] as quoted in [5] was used for this correlation. Then, the laminar flame speed S_L is estimated relative to the laminar flame speed of a stoichiometric mixture without any substitution for N_2, as in Equation A-21.

$$\left(S_L \middle/ S_{L,0} \right) = 1 - 2.52 \cdot \left(1 - T_{ad} \middle/ T_{ad,0} \right)^{0.684} \tag{A-21}$$

Here, the subscript 0 refers to the value at undisturbed conditions. For each mixture of fuel, air, oxygen, and diluent, CO_2 or Ar, the adiabatic flame temperature T_{ad} is calculated by a chemical equilibrium calculation.

Appendix B: Data and Operating Conditions

Tavg: average coolant temperature
Tair In.: intake runner air temperature
Texh: exhaust temperature
Airflow: flow of air through the manifold
COV: covariance of NIMEP
MAP Avg.: average manifold pressure over data file
ΔTexh.: exhaust temperature minus exhaust temperature at no jet flow divided by exhaust temperature at no jet flow
SL/S0: relative laminar flame speed

Baseline Data

Spark Timing CAD BTC	Tavg (C)	Tair In. (C)	Texh (C)	Airflow (g/s)	NIMEP (bar)	COV (%)	MAP Avg. (bar)
20	19.9	25.9	463	1.21	2.61	4.26	0.310
15	19.5	20.3	471	1.18	2.56	3.85	0.305
10	19.3	25.9	473	1.26	2.60	4.01	0.320
5	20.3	24.6	498	1.33	2.55	4.43	0.335
0	20.0	25.8	513	1.46	2.61	5.37	0.373
-5	19.7	23.1	550	1.59	2.60	6.27	0.411
-10	20.4	23.6	580	1.81	2.65	7.26	0.465
-15	20.0	23.4	617	2.11	2.54	8.86	0.533
-20	20.9	25.5	648	2.57	2.60	9.55	0.650

Spark Timing CAD BTC	Burn Duration			Combustion Phase		
	0-10%	0-50%	10-90%	CA 10%	CA 50%	CA 90%
20	15	26	17	175	186	192
15	17	26	16	182	191	198
10	16	26	18	186	196	204
5	19	29	18	194	204	212
0	20	31	20	200	211	220
-5	21	33	23	206	218	229
-10	22	35	25	212	225	237
-15	24	38	24	219	233	243
-20	27	44	30	227	244	257

Swirl Jet Data

Spark Timing CAD BTC	Airflow (g/s)	Jet Flow (g/s)	Jet Flow/ Total Flow	Tavg (C)	Tair In. (C)	Texh (C)	ΔTexh (C)
20	0	1.21	1.00	19.9	30.2	451	-2.7
20	0.09	1.13	0.93	19.5	28.5	455	-1.7
20	0.21	1.04	0.83	19.8	28.0	458	-1.1
20	0.34	0.95	0.74	19.8	28.4	457	-1.4
20	0.54	0.72	0.57	20.1	25.5	459	-0.9
20	0.64	0.59	0.48	19.7	23.1	452	-2.5
20	1.05	0.21	0.17	20.0	26.4	473	2.2
20	1.21	0	0.00	19.4	25.9	463	0.0
15	0	1.21	1.00	19.8	29.9	465	-1.3
15	0.11	1.13	0.91	19.5	28.1	466	-1.1
15	0.34	0.95	0.74	19.7	28.8	469	-0.4
15	0.54	0.72	0.57	19.9	26.6	471	0.0
15	0.65	0.59	0.48	20.2	24.9	474	0.7
15	0.83	0.4	0.33	19.3	24.0	464	-1.6
15	1	0.21	0.17	20.0	21.7	478	1.4
15	1.18	0	0.00	19.5	20.3	471	0.0
10	0	1.24	1.00	20.3	28.3	485	2.5
10	0.14	1.13	0.89	19.8	29.6	481	1.6
10	0.36	0.95	0.73	19.7	28.3	478	0.9
10	0.46	0.81	0.64	20.0	27.6	480	1.4
10	0.54	0.72	0.57	20.3	27.7	480	1.5
10	0.76	0.5	0.40	20.2	22.1	484	2.3
10	1.09	0.21	0.16	19.7	26.3	478	0.9
10	1.26	0	0.00	19.3	25.9	473	0.0
5	0.00	1.36	1.00	19.6	30.3	483	-3.1
5	0.05	1.25	0.96	20.1	30.5	495	-0.6
5	0.17	1.18	0.87	19.1	28.8	484	-2.8
5	0.22	1.13	0.84	19.7	28.2	486	-2.5
5	0.33	1.04	0.76	19.9	28.2	483	-3.0
5	0.53	0.81	0.60	20.0	28.1	489	-1.8
5	0.64	0.72	0.53	20.0	25.9	482	-3.4
5	0.69	0.64	0.48	20.0	26.6	484	-2.9
5	0.93	0.4	0.30	20.0	24.5	492	-1.2
5	1.33	0	0.00	20.3	24.6	498	0.0
0	0	1.46	1.00	19.6	31.1	500	-2.4
0	0.11	1.32	0.92	18.9	28.7	494	-3.6
0	0.15	1.3	0.90	19.3	28.8	500	-2.4
0	0.27	1.21	0.82	19.9	26.1	501	-2.3
0	0.37	1.13	0.75	19.9	26.6	502	-2.0
0	0.44	1.04	0.70	20.0	27.7	502	-2.0
0	0.58	0.89	0.61	19.9	27.6	499	-2.7
0	0.71	0.72	0.50	20.2	27.8	501	-2.4
0	0.9	0.5	0.36	20.5	26.9	508	-0.9
0	1.03	0.4	0.28	20.5	26.6	508	-0.9
0	1.26	0.21	0.14	20.1	25.9	508	-0.9
0	1.46	0	0.00	20.0	25.8	513	0.0

Spark Timing CAD BTC	Airflow (g/s)	Jet Flow (g/s)	Jet Flow/ Total Flow	Tavg (C)	Tair In. (C)	Texh (C)	ΔTexh (C)
-5	0	1.67	1.00	19.9	29.6	530	-3.6
-5	0	1.61	1.00	20.1	31.1	531	-3.5
-5	0.12	1.49	0.93	20.2	29.7	528	-4.0
-5	0.25	1.36	0.84	19.5	28.2	526	-4.3
-5	0.42	1.24	0.75	20.9	29.1	545	-0.9
-5	0.53	1.13	0.68	19.8	27.9	542	-1.4
-5	0.58	1.04	0.64	19.8	28.0	538	-2.2
-5	0.79	0.805	0.50	20.0	27.5	535	-2.6
-5	0.96	0.64	0.40	20.3	26.9	538	-2.2
-5	1.01	0.4	0.28	21.3	26.9	512	-6.9
-5	1.32	0.21	0.14	19.4	25.5	504	-8.4
-5	1.59	0	0.00	19.7	23.1	550	0.0
-10	0.01	1.85	0.99	19.7	31.2	562	-3.1
-10	0.07	1.73	0.96	20.4	28.4	552	-4.9
-10	0.20	1.61	0.89	19.6	30.3	566	-2.5
-10	0.49	1.36	0.74	20.4	29.4	568	-2.1
-10	0.61	1.21	0.66	19.5	27.1	571	-1.6
-10	0.69	1.13	0.62	19.9	27.9	571	-1.6
-10	0.75	1.04	0.58	19.5	27.4	571	-1.6
-10	1.11	0.64	0.37	21.3	27.4	555	-4.4
-10	1.56	0.21	0.12	20.8	25.7	569	-1.9
-10	1.81	0	0.00	20.4	23.6	580	0.0
-15	0	2.2	1.00	20.4	33.2	603	-2.3
-15	0.02	2.12	0.99	20.1	32.0	597	-3.2
-15	0.15	1.99	0.93	20.4	31.5	600	-2.7
-15	0.23	1.92	0.89	20.0	30.2	600	-2.7
-15	0.45	1.79	0.80	19.9	28.6	600	-2.8
-15	0.64	1.49	0.70	19.9	28.5	599	-2.8
-15	0.86	1.24	0.59	20.5	27.1	617	0.1
-15	0.94	1.15	0.55	20.7	26.6	609	-1.3
-15	1.04	0.97	0.48	20.9	28.3	610	-1.1
-15	1.36	0.64	0.32	19.6	27.1	610	-1.1
-15	1.87	0.21	0.10	20.7	25.6	610	-1.0
-15	2.11	0	0.00	20.0	23.4	617	0.0
-20	0	2.39	1.00	20.5	22.8	644	-0.6
-20	0.15	2.45	0.94	20.3	32.1	644	-0.7
-20	0.24	2.37	0.91	20.3	31.0	645	-0.5
-20	0.35	2.28	0.87	20.3	30.0	643	-0.8
-20	0.57	1.99	0.78	21.7	28.7	652	0.6
-20	0.79	1.79	0.69	20.2	29.3	644	-0.7
-20	0.92	1.61	0.64	20.6	28.5	648	0.0
-20	0.99	1.49	0.60	20.6	27.8	653	0.7
-20	1.11	1.36	0.55	20.0	26.6	644	-0.7
-20	1.26	1.15	0.48	20.1	26.8	645	-0.5
-20	1.43	0.97	0.40	20.5	27.9	638	-1.6
-20	2.35	0.21	0.08	19.8	25.4	642	-0.9
-20	2.57	0	0.00	20.9	25.5	648	0.0

Spark Timing CAD BTC	NIMEP (bar)	COV (%)	MAP Avg. (bar)	Burn Duration			Combustion Phase		
				0-10%	0-50%	10-90%	CA 10%	CA 50%	CA 90%
20	2.57	2.92	0.26	12	21	14	172	181	186
20	2.62	2.93	0.26	12	22	15	172	182	187
20	2.61	2.86	0.27	13	22	14	173	182	187
20	2.65	3.07	0.27	13	22	14	173	182	187
20	2.62	2.90	0.28	12	21	14	172	181	186
20	2.60	3.66	0.28	14	24	16	174	184	190
20	2.64	3.89	0.31	15	25	17	175	185	192
20	2.61	4.26	0.31	15	26	17	175	186	192
15	2.62	2.92	0.261	13	20	13	178	185	191
15	2.63	2.87	0.265	13	21	14	178	186	192
15	2.65	2.69	0.274	13	21	14	178	186	192
15	2.61	2.76	0.278	12	20	14	177	185	191
15	2.59	3.09		14	23	14	179	188	193
15	2.61	3.06		16	24	14	181	189	195
15	2.54	3.78		17	26	15	182	191	197
15	2.56	3.85	0.305	17	26	16	182	191	198
10	2.56	3.58	0.268	13	22	16	183	192	199
10	2.65	3.07	0.275	14	22	14	184	192	198
10	2.62	2.74	0.279	14	22	14	184	192	198
10	2.55	2.91	0.276	12	20	14	182	190	196
10	2.55	3.07	0.279	12	21	14	182	191	196
10	2.56	2.94	0.294	15	25	17	185	195	202
10	2.63	4.01	0.318	16	26	18	186	196	204
10	2.60	4.01	0.32	16	26	18	186	196	204
5	2.62	3.70	0.288	14	23	17	189	198	206
5	2.64	3.30	0.285	14	22	15	189	197	204
5	2.58	4.25	0.296	15	25	18	190	200	208
5	2.59	3.88	0.289	15	24	16	190	199	206
5	2.60	3.50	0.292	15	24	15	190	199	205
5	2.60	3.06	0.292	13	22	16	188	197	204
5	2.63	3.36	0.310	15	23	15	190	198	205
5	2.60	3.05	0.306	16	23	14	191	198	205
5	2.56	3.64	0.317	18	26	14	193	201	207
5	2.55	4.43	0.335	19	29	18	194	204	212
0	2.57	4.27	0.31	17	27	19	197	207	216
0	2.63	3.59	0.309	15	25	18	195	205	213
0	2.63	3.83	0.309	15	24	17	195	204	212
0	2.60	4.51	0.315	17	26	17	197	206	214
0	2.57	4.36	0.317	17	26	16	197	206	213
0	2.63	3.68	0.319	16	25	18	196	205	214
0	2.57	4.00	0.328	16	26	18	196	206	214
0	2.57	4.11	0.329	16	25	17	196	205	213
0	2.59	4.50	0.338	18	27	17	198	207	215
0	2.65	4.55	0.35	18	27	18	198	207	216
0	2.61	5.14	0.362	19	29	19	199	209	218
0	2.61	5.37	0.373	20	31	20	200	211	220

Spark Timing CAD BTC	NIMEP (bar)	COV (%)	MAP Avg. (bar)	Burn Duration			Combustion Phase		
				0-10%	0-50%	10-90%	CA 10%	CA 50%	CA 90%
-5	2.64	5.03	0.353	18	31	24	203	216	227
-5	2.60	4.94	0.35	18	30	23	203	215	226
-5	2.60	4.92	0.36	18	30	22	203	215	225
-5	2.65	4.85	0.361	17	28	22	202	213	224
-5	2.62	5.43	0.366	18	29	22	203	214	225
-5	2.60	4.92	0.354	17	29	21	202	214	223
-5	2.60	4.47	0.355	17	29	22	202	214	224
-5	2.65	4.30	0.373	18	29	21	203	214	224
-5	2.61	5.19	0.377	18	29	22	203	214	225
-5	2.64	4.05	0.347	13	23	19	198	208	217
-5	2.58	5.20	0.366	14	26	22	199	211	221
-5	2.60	6.27	0.411	21	33	23	206	218	229
-10	2.59	6.06	0.401	19	32	23	209	222	232
-10	2.58	5.92	0.41	19	33	25	209	223	234
-10	2.58	6.20	0.41	19	32	24	209	222	233
-10	2.63	5.95	0.413	18	30	21	208	220	229
-10	2.55	5.77	0.402	18	30	22	208	220	230
-10	2.65	4.79	0.409	17	30	24	207	220	231
-10	2.64	4.63	0.408	18	31	23	208	221	231
-10	2.62	5.78	0.434	20	32	22	210	222	232
-10	2.54	6.68	0.443	21	34	25	211	224	236
-10	2.65	7.26	0.465	22	35	25	212	225	237
-15	2.59	6.91	0.467	20	36	27	215	231	242
-15	2.56	7.08	0.473	21	37	28	216	232	244
-15	2.60	6.56	0.475	21	36	25	216	231	241
-15	2.60	6.58	0.476	21	36	27	216	231	243
-15	2.60	6.50	0.481	21	36	26	216	231	242
-15	2.67	7.29	0.484	21	35	25	216	230	241
-15	2.62	7.38	0.493	21	34	25	216	229	241
-15	2.60	7.54	0.494	21	36	26	216	231	242
-15	2.64	5.83	0.484	21	34	24	216	229	240
-15	2.62	7.22	0.501	21	35	26	216	230	242
-15	2.56	8.00	0.521	24	38	25	219	233	244
-15	2.54	8.86	0.533	24	38	24	219	233	243
-20	2.60	6.88		21	37	28	221	237	249
-20	2.64	7.60	0.572	23	41	31	223	241	254
-20	2.60	7.86	0.516	25	43	33	225	243	258
-20	2.63	7.78	0.578	24	41	30	224	241	254
-20	2.52	8.02	0.578	25	43	31	225	243	256
-20	2.63	8.91	0.581	24	40	30	224	240	254
-20	2.57	9.95	0.597	25	43	33	225	243	258
-20	2.55	10.20	0.599	25	42	31	225	242	256
-20	2.55	9.47	0.596	24	42	32	224	242	256
-20	2.62	7.52	0.582	23	38	27	223	238	250
-20	2.64	7.93	0.589	24	40	28	224	240	252
-20	2.55	9.19	0.633	27	44	29	227	244	256
-20	2.60	9.55	0.65	27	44	30	227	244	257

Tumble Jet Data

Spark Timing CAD BTC	Airflow (g/s)	Jet Flow (g/s)	Jet Flow/ Total Flow	Tavg (C)	Tair In. (C)	Texh (C)	ΔTexh (C)
20	0.00	1.30	1.00	20.6	34.1	464	0.4
20	0.20	1.13	0.85	20.5	31.9	459	-0.7
20	0.56	0.81	0.59	20.8	31.2	468	1.2
20	0.70	0.64	0.48	20.7	29.9	471	1.8
20	0.99	0.31	0.24	19.8	26.0	464	0.4
20	1.19	0.00	0.00	19.5	25.0	462	0.0
15	0.32	1.04	0.76	20.5	32.5	463	-2.1
15	0.46	0.89	0.66	20.5	31.8	472	-0.3
15	0.60	0.72	0.55	20.4	30.4	477	0.8
15	0.99	0.31	0.24	20.5	26.3	475	0.4
15	1.21	0.00	0.00	20.3	25.6	473	0.0
10	0.00	1.36	1.00	20.3	33.7	476	-1.5
10	0.31	1.04	0.77	20.4	32.9	478	-1.2
10	0.63	0.72	0.53	20.1	30.3	487	0.8
10	1.03	0.31	0.23	20.7	26.6	479	-0.8
10	1.27	0.00	0.00	20.5	25.9	483	0.0
5	0.00	1.36	1.00	20.6	34.8	499	2.7
5	0.14	1.21	0.90	20.5	34.2	499	2.7
5	0.49	0.95	0.66	20.6	31.8	488	0.3
5	0.78	0.64	0.45	19.7	29.5	503	3.4
5	1.08	0.31	0.22	20.6	26.8	490	0.9
5	1.33	0.00	0.00	20.5	26.1	486	0.0
0	0.09	1.49	0.94	21.0	34.1	507	-1.6
0	0.29	1.21	0.81	20.7	33.9	511	-1.0
0	0.49	1.04	0.68	20.8	32.5	508	-1.6
0	0.80	0.72	0.47	20.1	29.6	517	0.2
0	1.21	0.31	0.20	19.9	26.5	521	1.1
0	1.46	0.00	0.00	20.4	26.1	516	0.0
-5	0.06	1.59	0.96	20.5	35.9	542	-2.7
-5	0.40	1.36	0.77	20.9	33.3	543	-2.6
-5	0.54	1.13	0.68	20.7	32.3	534	-4.2
-5	0.87	0.81	0.48	20.6	29.6	550	-1.2
-5	1.39	0.31	0.18	19.5	26.4	555	-0.4
-5	1.65	0.00	0.00	19.4	25.9	557	0.0
-10	0.00	1.87	1.00	20.7	36.9	582	-1.4
-10	0.34	1.61	0.83	20.9	34.2	575	-2.5
-10	0.61	1.21	0.66	20.8	32.3	567	-3.8
-10	1.04	0.81	0.44	20.7	28.8	591	0.2
-10	1.62	0.31	0.16	19.8	26.3	593	0.5
-10	1.86	0.00	0.00	19.6	26.5	590	0.0
-15	0.09	2.12	0.96	21.0	36.9	626	-0.6
-15	0.28	1.92	0.87	20.8	35.5	625	-0.7
-15	0.73	1.49	0.67	20.8	32.3	609	-3.2
-15	1.18	0.97	0.45	21.1	28.1	623	-1.0
-15	1.66	0.57	0.26	21.0	26.2	629	-0.1
-15	2.31	0.00	0.00	20.0	25.7	630	0.0

Spark Timing CAD BTC	Airflow (g/s)	Jet Flow (g/s)	Jet Flow/ Total Flow	Tavg (C)	Tair In. (C)	Texh (C)	ΔTexh (C)
-20	0.27	2.37	0.90	21.0	36.2	661	-1.2
-20	0.55	2.12	0.79	21.0	34.1	653	-2.3
-20	1.12	1.36	0.55	21.2	30.2	647	-3.2
-20	1.90	0.64	0.25	20.9	26.8	664	-0.7
-20	2.69	0.00	0.00	21.0	25.7	669	0.0

Spark Timing BTC	NIMEP (bar)	COV (%)	MAP Avg. (bar)	Burn Duration			Combustion Phase		
				0-10%	0-50%	10-90%	CA 10%	CA 50%	CA 90%
20	2.57	4.38	0.264	13	18	10	173	178	183
20	2.59	4.46	0.27	14	19	10	174	179	184
20	2.65	4.1	0.276	15	21	11	175	181	186
20	2.66	3.63	0.282	17	22	11	177	182	188
20	2.63	3.19	0.286	19	27	15	179	187	194
20	2.63	3.55							
15	2.68	4.03	0.277	13	20	12	178	185	190
15	2.55	3.8	0.265	15	21	12	180	186	192
15	2.55	3.37	0.27	14	21	13	179	186	192
15	2.58	3.27	0.291	17	27	18	182	192	200
15	2.56	4.02	0.298	19	28	16	184	193	200
10	2.63	3.13	0.265	12	19	13	182	189	195
10	2.63	3.74	0.278	14	20	11	184	190	195
10	2.57	3.31	0.278	14	21	13	184	191	197
10	2.63	3.25	0.303	15	24	15	185	194	200
10	2.58	4.5	0.312	19	29	18	189	199	207
5	2.64	2.72	0.277	13	20	12	188	195	200
5	2.58	2.96	0.278	13	20	13	188	195	201
5	2.67	4	0.298	14	22	15	189	197	204
5	2.63	3.34	0.302	14	23	16	189	198	205
5	2.58	4.25	0.317	15	26	19	190	201	209
5	2.56	4.82	0.325	16	27	20	191	202	211
0	2.65	3.96	0.322	17	25	15	197	205	212
0	2.64	3.31	0.31	16	24	15	196	204	211
0	2.60	4	0.315	17	25	15	197	205	212
0	2.66	3.63	0.327	17	26	16	197	206	213
0	2.62	5.42	0.354	18	30	24	198	210	222
0	2.60	5.57	0.358	17	30	25	197	210	222
-5	2.61	4.22	0.348	16	28	22	201	213	223
-5	2.61	4.46	0.361	17	28	21	202	213	223
-5	2.61	3.92	0.349	17	27	18	202	212	220
-5	2.63	4.9	0.363	17	28	21	202	213	223
-5	2.66	5.89							
-5	2.66	6.31	0.406	20	33	26	205	218	231
-10	2.58	6.19	0.391	17	30	24	207	220	231
-10	2.61	5.16	0.402	17	30	24	207	220	231
-10	2.61	4.27	0.387	16	28	22	206	218	228
-10	2.62	5.05	0.413	17	31	24	207	221	231
-10	2.65	6.64	0.454	19	35	28	209	225	237
-10	2.66	6.67	0.459	20	35	28	210	225	238

Spark Timing BTC	NIMEP (bar)	COV (%)	MAP avg. (bar)	Burn Duration			Combustion Phase		
				0-10%	0-50%	10-90%	CA 10%	CA 50%	CA 90%
-15	2.67	6.3	0.477	20	36	29	215	231	244
-15	2.66	6.57	0.479	20	36	29	215	231	244
-15	2.65	5.26	0.478	19	35	29	214	230	243
-15	2.66	5.86	0.488	20	35	27	215	230	242
-15	2.67	6.65	0.518	22	38	29	217	233	246
-15	2.65	7.45	0.556	23	42	34	218	237	252
-20	2.62	8.26	0.573	23	41	31	223	241	254
-20	2.60	7.73	0.5778	23	41	32	223	241	255
-20	2.54	7.19	0.566	22	40	31	222	240	253
-20	2.54	7.26	0.594	25	43	31	225	243	256
-20	2.65	8.69	0.65	26	45	34	226	245	260

Laminar Flame Speed Change Data

Spark Timing CAD BTC	S_L/S_0	Tavg (C)	Tair In. (C)	Texh (C)	MAP Avg. (bar)	NIMEP (bar)	COV (%)
CO_2							
20	1.00	20.3	25.0	448	0.29	2.60	4.24
20	0.90	20.1	25.0	467	0.30	2.66	4.18
20	0.85	20.5	24.9	471	0.30	2.58	5.53
20	0.81	20.1	25.4	506	0.29	2.55	5.09
20	0.79	20.6	26.5	531	0.37	2.66	8.23
20	0.77	20.6	26.2	548	0.39	2.67	8.85
Ar							
20	1.00	20.3	25.0	448	0.29	2.60	4.24
20	1.34	20.3	25.8	465	0.27	2.58	4.21
20	1.43	20.5	26.1	467	0.26	2.55	4.14
20	1.52	20.6	25.1	462	0.26	2.66	4.23
20	1.62	20.7	25.4	444	0.25	2.52	3.95
20	1.65	20.3	24.8	416	0.26	2.54	4.39
20	1.76	19.9	25.4	404	0.26	2.55	4.35
20	1.82	19.7	25.7	397	0.26	2.61	4.00
CO_2							
15	1.00	20.3	24.0	468	0.30	2.65	4.48
15	0.91	19.9	25.6	468	0.30	2.58	4.64
15	0.84	20.4	25.5	481	0.32	2.57	6.56
15	0.78	20.5	26.1	546	0.39	2.68	8.11
Ar							
15	1.00	20.3	24.0	468	0.30	2.65	4.48
15	1.35	19.3	24.9	451	0.27	2.60	3.82
15	1.53	19.9	24.1	449	0.25	2.55	4.22
15	1.66	20.3	22.6	390	0.26	2.53	3.98
15	1.80	21.0	23.5	392	0.26	2.59	4.09
15	1.87	19.7	23.9	375	0.26	2.61	3.92
CO_2							
10	1.00	20.5	23.8	471	0.31	2.64	3.68
10	0.91	20.1	25.6	477		2.60	5.12
10	0.80	20.7	26.0	520	0.32	2.64	5.62
10	0.81	20.5	26.4	535	0.32	2.68	4.69
10	0.79	20.6	25.6	571	0.42	2.57	9.56
Ar							
10	1.00	20.5	23.8	471	0.31	2.64	3.68
10	1.34	21.0	24.5	480	0.28	2.64	3.55
10	1.53	20.0	22.9	464	0.26	2.62	3.66
10	1.66	21.4	24.4	464	0.26	2.62	3.25
10	1.81	21.1	25.1	435	0.25	2.60	3.26
10	1.89	20.9	25.3	403	2.52	2.59	3.76

Spark Timing CAD BTC	S_L/S_0	Tavg (C)	Tair In. (C)	Texh (C)	MAP Avg. (bar)	NIMEP (bar)	COV (%)
CO_2							
5	1.00	20.5	23.4	489	0.32	2.57	4.85
5	0.90	20.2	25.8	497	3.38	2.58	5.47
5	0.87	20.4	25.9	517	0.36	2.64	5.74
5	0.84	20.4	25.4	537	0.37	2.60	6.94
5	0.80	20.3	25.4	579	0.45	2.54	11.17
5	0.79	20.4	25.8	589	0.47	2.60	12.48
Ar							
5	1.00	20.5	23.4	489	0.32	2.57	4.85
5	1.34	19.4	25.2	477	0.29	2.61	3.75
5	1.52	19.7	25.4	484	0.27	2.62	3.27
5	1.60	21.4	25.9	492	0.25	2.58	3.44
5	1.80	20.8	25.2	452	0.26	2.62	3.22
5	1.88	20.6	25.1	438	0.25	2.59	3.02
CO_2							
0	1.00	20.1	23.7	503	0.36	2.62	5.79
0	0.91	20.6	26.1	532	0.38	2.68	5.85
0	0.87	20.5	25.9	562	0.39	2.58	6.43
0	0.83	20.9	24.7	573	0.38	2.59	7.39
0	0.81	20.7	24.6	579	0.39	2.65	7.09
0	0.80	21.1	25.2	593	0.39	2.62	7.54
0	0.81	20.7	24.7	603	0.46	2.66	9.15
0	0.81	20.5	26.3	611	0.49	2.52	11.33
0	0.77	20.7	26.2	623	0.51	2.59	11.84
Ar							
0	1.00	20.1	23.7	503	0.36	2.62	5.79
0	1.32	20.2	25.8	502	0.31	2.58	4.23
0	1.50	20.3	26.0	503	0.29	2.60	3.07
0	1.64	20.6	24.8	474	0.28	2.53	2.93
0	1.76	20.8	25.4	477	0.28	2.68	2.95
0	1.83	20.9	26.0	480	0.26	2.63	2.59
CO_2							
-5	1.00	20.1	26.0	539	0.40	2.56	6.96
-5	0.88	20.7	26.3	586	0.44	2.65	7.18
-5	0.86	20.6	26.2	599	0.46	2.58	8.95
-5	0.84	21.0	25.8	614	0.46	2.54	9.40
-5	0.81	20.7	24.2	630	0.52	2.60	11.24
-5	0.81	20.5	26.3	633	0.55	2.56	12.78
-5	0.81	20.6	25.9	639	0.58	2.69	12.38
Ar							
-5	1.00	20.1	26.0	539	0.40	2.56	6.96
-5	1.31	19.8	25.4	522	0.35	2.67	4.76
-5	1.48	20.3	25.2	517	0.32	2.64	3.49
-5	1.60	20.6	25.7	503	0.32	2.61	3.49
-5	1.72	20.8	25.3	491	0.30	2.64	2.95
-5	1.82	20.8	25.5	485	0.28	2.58	2.67

Spark Timing CAD BTC	S_L/S_0	Tavg (C)	Tair In. (C)	Texh (C)	MAP Avg. (bar)	NIMEP (bar)	COV (%)
CO_2							
-10	1.00	21.2	25.0	586	0.46	2.66	6.98
-10	0.92	20.7	26.4	597	0.49	2.66	7.19
-10	0.88	20.9	26.4	619	0.51	2.63	8.43
-10	0.86	20.9	26.5	630	0.52	2.59	9.69
-10	0.84	20.8	24.7	632	0.48	2.51	8.55
-10	0.83	20.2	24.6	634	0.51	2.60	8.92
-10	0.83	20.4	22.8	663	0.61	2.58	13.06
-10	0.82	21.0	25.8	673	0.67	2.69	13.30
Ar							
-10	1.00	21.2	25.0	586	0.46	2.66	6.98
-10	1.44	20.5	25.1	558	0.37	2.66	4.16
-10	1.58	20.0	25.8	537	0.36	2.56	4.59
-10	1.76	20.5	26.5	510	0.32	2.64	2.99
-10	1.90	20.0	21.2	504	0.27	2.65	2.66
CO_2							
-15	1.00	20.4	25.5	628	0.54	2.67	7.55
-15	0.93	21.6	27.0	647	0.56	2.54	9.68
-15	0.90	21.0	26.6	660	0.61	2.61	10.02
-15	0.88	21.0	26.7	667	0.62	2.52	11.17
-15	0.84	21.3	25.0	692	0.71	2.62	13.60
-15	0.84	22.9	25.9	695	0.75	2.65	14.07
-15	0.83	20.6	25.5	698	0.78	2.65	14.29
Ar							
-15	1.00	20.4	25.5	628	0.54	2.67	7.55
-15	1.33	20.9	23.6	598	0.45	2.62	5.39
-15	1.42	21.1	24.2	592	0.42	2.60	4.45
-15	1.49	20.5	25.3	593	0.40	2.61	4.65
-15	1.53	21.2	26.4	591	0.41	2.57	4.61
-15	1.65	19.3	26.6	568	0.39	2.67	3.60
-15	1.71	19.4	26.7	552	0.38	2.65	3.60
-15	1.82		23.2	549	0.32	2.68	2.65
-15	1.85	20.1	22.7	536	0.31	2.66	2.63
CO_2							
-20	1.00	21.6	25.7	670	0.64	2.57	9.09
-20	0.92	21.3	26.4	684	0.68	2.64	10.05
-20	0.86	20.7	24.3	694	0.73	2.63	10.63
-20	0.85	23.6	25.6	720	0.72	2.60	11.31
-20	0.85	21.2	25.5	719	0.82	2.56	13.37
-20	0.85	22.6	25.6	723	0.87	2.66	14.25
-20	0.84	20.4	25.7	706	0.88	2.55	14.76
Ar							
-20	1.00	21.6	25.7	670	0.64	2.57	9.09
-20	1.44	18.9	22.1	632	0.48	2.65	4.87
-20	1.59	20.1	26.4	603	0.46	2.66	4.25
-20	1.65	19.6	26.5	584	0.45	2.59	4.14
-20	1.75	19.7	23.3	577	0.37	2.60	2.94
-20	1.78	20.4	23.4	588	0.37	2.66	3.06
-20	1.87	20.9	23.9	580	0.34	2.63	2.51

Spark Timing CAD BTC	Burn Duration			Combustion Phasing		
	0-10%	0-50%	10-90%	CA 10%	CA 50%	CA 90%
CO_2						
20	12	23	18	172	183	190
20	15	26	18	175	186	193
20	18	29	19	178	189	197
20	19	29	18	179	189	197
20	28	44	40	188	204	228
20	31	48	44	191	208	235
Ar						
20	12	23	18	172	183	190
20	9	19	15	169	179	184
20	9	17	13	169	177	182
20	11	17	11	171	177	182
20	10	16	10	170	176	180
20	11	17	10	171	177	181
20	11	16	9	171	176	180
20	11	16	9	171	176	180
CO_2						
15	15	24	16	180	189	196
15	16	26	18	181	191	199
15	19	30	22	184	195	206
15	26	44	42	191	209	233
Ar						
15	15	24	16	180	189	196
15	11	19	14	176	184	190
15	11	17	11	176	182	187
15	10	17	12	175	182	187
15	9	15	10	174	180	184
15	8	14	10	173	179	183
CO_2						
10	14	24	18	184	194	202
10	16	28	21	186	198	207
10	17	28	21	187	198	208
10	17	28	21	187	198	208
10	27	46	43	197	216	240
Ar						
10	14	24	18	184	194	202
10	12	20	14	182	190	196
10	9	16	13	179	186	192
10	9	17	13	179	187	192
10	9	15	10	179	185	189
10	7	14	11	177	184	188

Spark Timing CAD BTC	Burn Duration 0-10%	0-50%	10-90%	Combustion Phasing CA 10%	CA 50%	CA 90%
CO_2						
5	16	27	20	191	202	211
5	17	28	20	192	203	212
5	19	31	24	194	206	218
5	20	34	27	195	209	222
5	28	49	46	203	224	249
5	29	51	48	204	226	252
Ar						
5	16	27	20	191	202	211
5	13	23	17	188	198	205
5	11	19	14	186	194	200
5	10	17	12	185	192	197
5	8	15	12	183	190	195
5	8	15	11	183	190	194
CO_2						
0	18	29	21	198	209	219
0	19	30	21	199	210	220
0	21	34	26	201	214	227
0	21	34	26	201	214	227
0	22	35	25	202	215	227
0	22	35	25	202	215	227
0	27	45	41	207	225	248
0	28	48	44	208	228	252
0	29	50	45	209	230	254
Ar						
0	18	29	21	198	209	219
0	16	25	17	196	205	213
0	14	22	14	194	202	208
0	14	22	14	194	202	208
0	11	18	13	191	198	204
0	11	17	11	191	197	202
CO_2						
-5	22	33	22	207	218	229
-5	22	36	27	207	221	234
-5	24	40	32	209	225	241
-5	24	40	33	209	225	242
-5	26	47	43	211	232	254
-5	28	49	43	213	234	256
-5	29	50	42	214	235	256
Ar						
-5	22	33	22	207	218	229
-5	17	26	17	202	211	219
-5	15	23	15	200	208	215
-5	15	23	16	200	208	216
-5	14	21	13	199	206	212
-5	12	18	11	197	203	208

Spark Timing CAD BTC	Burn Duration 0-10%	0-50%	10-90%	Combustion Phasing CA 10%	CA 50%	CA 90%
CO$_2$						
-10	21	34	24	211	224	235
-10	22	36	26	212	226	238
-10	24	40	31	214	230	245
-10	25	43	33	215	233	248
-10	23	39	30	213	229	243
-10	24	40	30	214	230	244
-10	28	51	44	218	241	262
-10	31	54	44	221	244	265
Ar						
-10	21	34	24	211	224	235
-10	16	26	18	206	216	224
-10	16	27	19	206	217	225
-10	13	22	15	203	212	218
-10	9	16	11	199	206	210
CO$_2$						
-15	23	39	28	218	234	246
-15	26	43	30	221	238	251
-15	27	46	35	222	241	257
-15	28	48	38	223	243	261
-15	31	53	41	226	248	267
-15	33	56	42	228	251	270
-15	36	58	40	231	253	271
Ar						
-15	23	39	28	218	234	246
-15	19	31	22	214	226	236
-15	18	30	20	213	225	233
-15	17	28	19	212	223	231
-15	18	29	20	213	224	233
-15	16	26	18	211	221	229
-15	15	25	18	210	220	228
-15	11	19	14	206	214	220
-15	11	19	13	206	214	219
CO$_2$						
-20	27	45	33	227	245	260
-20	28	46	32	228	246	260
-20	30	50	36	230	250	266
-20	31	50	34	231	250	265
-20	40	59	34	240	259	274
-20	41	59	34	241	259	275
-20	45	62	31	245	262	276
Ar						
-20	27	45	33	227	245	260
-20	20	32	22	220	232	242
-20	18	30	21	218	230	239
-20	18	29	19	218	229	237
-20	14	23	16	214	223	230
-20	12	22	16	212	222	228
-20	12	20	13	212	220	225